Closed-loop Controlled Filament Stretching and Break-up of Polymer Solutions

by

Roger Yeh

Bachelor of Science in Mechanical Engineering
and Applied Mathematics
Massachusetts Institute of Technology, 2002

Submitted to the Department of Mechanical Engineering
in partial fulfillment of the requirements for the degree of

Master of Science in Mechanical Engineering

at the

MASSACHUSETTS INSTITUTE OF TECHNOLOGY

June 2005

Author .....
Department of Mechanical Engineering
May 21, 2005

Certified by .....
Gareth H. McKinley
Professor of Mechanical Engineering
Thesis Supervisor

Accepted by .....
Lallit Anand
Professor of Mechanical Engineering
Chairman, Department Committee on Graduate Students

Closed-loop Controlled Filament Stretching and Break-up of Polymer Solutions

by

Roger Yeh

Submitted to the Department of Mechanical Engineering
on May 21, 2005, in partial fulfillment of the
requirements for the degree of
Master of Science in Mechanical Engineering

Abstract

A constant true (radial) strain rate filament stretching experiment has been the Holy Grail of extensional rheological studies. These experiments are performed on a *Fi*lament *S*tretching *E*xtensional *R*heometer (FiSER). A filament stretching experiment is the only direct way of measuring the extensional viscosity of a fluid. Previous attempts to achieve constant rate stretching have required tedious and iterative processes, which relied on the data of previous experiments to generate an axial profile that would result in a constant true strain rate experiment. This study presents a method to actively control the axial strains via the utilization of radial strain feedback. The first method we tried was an "Euler 1st order approximation," in which the ratio of the axial and radial strains is calculated at each time-step to determine the axial strain necessary at the next time-step to maintain a constant radial strain rate. This method worked, but was limited by how accurate this "ratio" of strains could be calculated. The "ratio" becomes unstable when the change in strain per time-step reaches the same order of noise. To fix this problem, we implemented a least squares linear regression scheme. With this algorithm, we were able to reach radial strains of $\varepsilon_D \sim 7$ with strain rates of $0.8 < \dot{\varepsilon}_D < 5\ \mathrm{s}^{-1}$.

Finally, we compared stretch-to-break (STB) experiments of a Newtonian fluid, styrene oil, to theoretical model. These experiments are also done on FiSER with the nominal strain rate held constant, generally very low ($\dot{\varepsilon}_D \sim 0.1\ \mathrm{s}^{-1}$). For a Newtonian fluid, the diameter decay can be determined analytically. We repeat the same with a weakly elastic fluid, STP® motor oil.

Thesis Supervisor: Gareth H. McKinley
Title: Professor of Mechanical Engineering

Acknowledgments

There have been many people who have helped me throughout my academic career. Many thanks to all of them. I would particularly like to thank my family, especially my mom and sister, for all their love and support. My good friends Brian, Grace, and Allen, were the best cheerleaders that no money can buy. My labmates in the Non-Newtonian Fluids group, especially Trevor and Giorgia, were very helpful in providing insight to my research as well as stress relief. Additional thanks goes to Fred in the Edgerton machine shop for putting up with me through all these years. May he finally "retire" for real. Finally, I want to thank my advisor, Gareth McKinley, for giving me the opportunity to work on this project. His guidance was vital in the progression and success of this study.

This research was supported by NASA Grant NNC-04GA41G.

Contents

List of Figures

List of Tables

Chapter 1

Introduction

Extensional rheology is relevant across many fields and applications. It is important whenever and wherever there is an extensional flow. Such flows come up in many commercial applications and has been the subject of many research topics in academia. In industry, spray coating, extrusions, and adhesive peeling are some of the processes that rely on extensional flows. In academia, Smith and Chu have used extensional flows to perform studies on DNA uncoiling and relaxation. Drop formation and contraction flows are also relevant topics with applications in the ink-jet printing industry. We now give a quick overview on some of the research that has been done on extensional flows.

Scientists have long been interested in studying the spinnability of biological fluids to mimic its processes. Thompson noted in his book, *On Growth and Form* [47],[1] that certain viscous fluids could be drawn into fine threads. He called such fluids to be "viscid." D'Arcy's term viscidity is now known more commonly as "spinnability," the ability of a fluid to form thin strands much like a spider spins its web or a silkworm spins its cocoon. It was first known by its German name, "Spinnbarkeit."[2] Burnett *et al.* [11] performed experiments on bovine cervical mucus and showed that the mucus is significantly more spinnable near estrus than other times in the cycle. The studies of Puchelle *et al.* [33] on bronchial mucus showed a relationship between spinnability

[1] First published in 1917.

[2] It was translated to "spinability" by Reiner and Scott-Blair.

and the transport velocity.

"Sprayability" is a another property involving extensional flows. Spraying processes are important in areas such as ink-jet printing and agricultural fertilization. Often times, when a drop of fluid is being ejected from a nozzle, the liquid bridge that connects the drop to the fluid in the nozzle will break and form secondary droplets. This causes undesirable marks in ink-jet printing and spraying over unwanted areas when fertilizer is sprayed from high above.

Fernando *et al.* [15] studied the extensional rheology of thickeners for roll and spray applications. They showed that using high molecular weight macro-molemcules that are flexible increases the the the misting in rolling applications but decreases atomization in spray applications.

Going back to ink-jet printing, drop formation has been an important process studied widely by many researchers. Chen and Basaran [12] showed a way to produce drops that are an order of magnitude smaller in volume compared to the conventional drops using the same nozzles. Shore and Harrison [39] further showed that adding polyethylene oxide (PEO) to a low viscosity Newtonian solvent can be useful as it suppresses satellite drops. Though the ink-jet printing industry is the area with the highest revenue generation, other important applications include DNA arraying, pipetting of fluids for drug discovery, and particle and microcapsule manufacturing [5].

McKinley's review [23] of visco-elasto-capillary thinning of complex fluids gives further applications of extensional rheology. Figure 1–1 shows various break-up phenomena of viscoelastic fluids. These include break-up of a high-speed fluid jet containing PEO, threads forming from cutting an okra, roll-coating of hydroxyethylcellulose (HEC), and beads-on-a-string morphology forming in an electro-spinning process.

The significance of extensional rheology in so many areas makes it an interesting and important area of study. In this thesis, we want to specifically study the relationship between stress and strain, as well as stress and strain rate, of a fluid in extensional flows.

More specifically, the extensional rheology of dilute polymer solutions is of signifi-

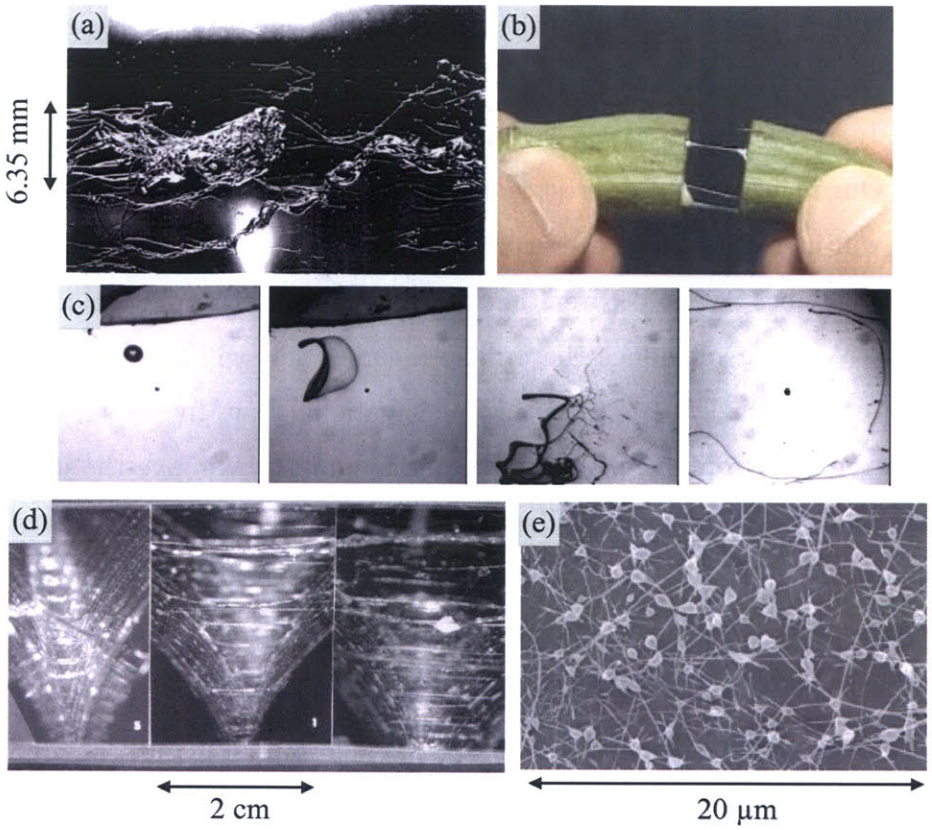

Figure 1–1: Examples of break-up phenomena - (a) break-up of a high-speed fluid jet containing PEO, (b) thin threads formed from cutting an ocra, (c) 'bag-break-up' atomization in a droplet ejected from a nozzle into high-spped cross-stream airflow, (d) high-speed forward roll-coating of hydroxyethylcellulose (HEC), and (e) beads-on-a-string morphology forming in an electro-spinning process. Taken with permission from McKinley [23].

cance because of its interesting properties. Concentrated polymer solutions experience very little hydrodynamic interactions and excluded volume effects. So in this sense, dilute solutions actually have more complexity than concentrated solutions. Concentrated solutions do, however, have the added complexity of self entanglement [18,19]. Furthermore, the solutions we use in this study are made from a monodisperse polymer. Though we do not compare solutions with varying molecular weights, these studies can be used to characterize polydisperse solutions. This is done by taking linear combinations of the monodisperse solutions, of which the polydisperse polymer

distribution is composed, and obtain rheological properties with the appropriate distribution. All of these are useful in characterizing polymers on the basis of molecular weight, stiffness, branching, and hydrodynamic interactions.

To study extensional rheology, we utilize a *Fi*lament *S*tretching *E*xtension *R*heometer (FiSER). Our main fluid of interest is a dilute polystyrene in oligameric styrene solvent. We will first cover some literature in chapter 2, where we discuss the basics of filament stretching. We will cover the stress and strain tensors specific to filament stretching. We then introduce the kinetic theories that will be used to model the visco-elastic response of the polymer in an elongational flow. In chapter 3, we discuss filament stretching from the view of an experimentalist. We give the details of the hardware that is used in the FiSER. We then go over the different types of filament stretching experiments. In chapter 4, we focus on the motion control of the FiSER. Previous control methods will be reviewed, as well as methods that were considered. We then introduce the Euler method that was used to achieve a constant true strain rate stretching experiment. The stability of this method motivates modifications to algorithm, which leads us to the least squares approximation method.

We present the rheological results in chapter 5, both shear and extensional. We compare the results with theory, again both in shear and extensional. We discuss the agreement and disagreement between the model and experimental data, and give conjectures to the differences. In chapter 6, we give results for stretch-to-break (STB) experiments. These experiments were done with a Newtonian fluid, styrene oil, as well as a weakly elastic fluid, STP® motor oil. We finally make concluding remarks in chapter 7.

Chapter 2

Literature Review

This chapter provides the theoretical background for extensional flows. We define flow field and geometries that are used. We introduce the polymer science used to model the fluid of interest. Finally, we define the dimensional numbers to show the competition between various effects present in the flow. For an introduction to elongational flows, with interesting historical notes on the early explorations and developments of extensional viscosities and other related material properties, see Petrie's book, *Elongational Flows* [30].

2.1 Elongational Flow

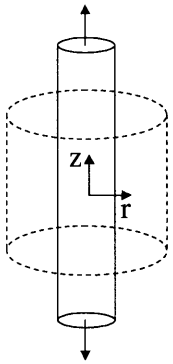

Figure 2–1: A fluid sample, simplified as a cylindrical body, being stretched uniaxially.

In our filament stretching experiments, we first consider a simplified version of the fluid kinematics where the flow geometry can be modelled as a cylinder being stretched in the axial direction. See figure 2–1. As it stretches in the z-axis, the cylinder gets thinner in the r-axis, or x- and y-axes. We can represent the velocity gradient of this flow as:

$$\nabla v = \begin{pmatrix} \frac{dv_x}{dx} & \frac{dv_x}{dy} & \frac{dv_x}{dz} \\ \frac{dv_y}{dx} & \frac{dv_y}{dy} & \frac{dv_y}{dz} \\ \frac{dv_z}{dx} & \frac{dv_z}{dy} & \frac{dv_z}{dz} \end{pmatrix} \tag{2.1}$$

For an elongation, or extensional, flow, the velocity field is given by:

$$v_x = -\frac{1}{2}\dot{\varepsilon}x \tag{2.2a}$$

$$v_y = -\frac{1}{2}\dot{\varepsilon}y \tag{2.2b}$$

$$v_z = \dot{\varepsilon}z \tag{2.2c}$$

where $\dot{\varepsilon}$ is the strain rate, which we will formally define in section 2.2.1. The resulting velocity gradient is then:

$$\nabla v = \begin{pmatrix} -\frac{1}{2}\dot{\varepsilon} & 0 & 0 \\ 0 & -\frac{1}{2}\dot{\varepsilon} & 0 \\ 0 & 0 & \dot{\varepsilon} \end{pmatrix} \tag{2.3}$$

The velocity gradient of an extensional flow is purely diagonal, meaning that the flow is shear-free. In the case of filament stretching, where there is axial symmetry,

we can easily represent the velocity field and gradient in cylindrical coordinates:

$$v_r = -\frac{1}{2}\dot{\varepsilon} r \tag{2.4a}$$

$$v_\theta = 0 \tag{2.4b}$$

$$v_z = \dot{\varepsilon} z \tag{2.4c}$$

As before, we can combine these velocities and represent them as a velocity gradient:

$$\nabla v = \begin{pmatrix} \frac{dv_r}{dr} & \frac{1}{r}\frac{dv_r}{d\theta} - \frac{v_\theta}{r} & \frac{dv_r}{dz} \\ \frac{dv_\theta}{dr} & \frac{1}{r}\frac{dv_\theta}{d\theta} + \frac{v_r}{r} & \frac{dv_\theta}{dz} \\ \frac{dv_z}{dr} & \frac{1}{r}\frac{dv_z}{d\theta} & \frac{dv_z}{dz} \end{pmatrix} = \begin{pmatrix} -\frac{1}{2}\dot{\varepsilon} & 0 & 0 \\ 0 & -\frac{1}{2}\dot{\varepsilon} & 0 \\ 0 & 0 & \dot{\varepsilon} \end{pmatrix} \tag{2.5}$$

The strain rate tensor then becomes:

$$\dot{\gamma} = \nabla v + \nabla v^T = \begin{pmatrix} -\dot{\varepsilon} & 0 & 0 \\ 0 & -\dot{\varepsilon} & 0 \\ 0 & 0 & 2\dot{\varepsilon} \end{pmatrix} \tag{2.6}$$

All of these equations are only valid for purely uniaxial stretching, where we can consider the fluid sample as a perfect cylinder. In reality, the fluid will *not* always deform in such a manner. For short times, $t \sim 0$, the velocity field is governed by lubrication theory. This means that the strain rates in the axial and radial direction will be different from that as given in equation 2.6, and will continue to change until the fluid begins to experience uniaxial stretching.

2.2 Mechanics

Before we can start discussing polymer physics, we need to define some of the geometries used in filament stretching experiments. We first establish the important dimensions in a generalized stretching experiment. We then show which measurements can

be made, and the material properties that can be calculated from these measurements.

2.2.1 Kinematics

Figure 2–2 shows a very general setup in a filament stretching experiment. The two important length scales are the plate separation, L, and mid-plane diameter, D. The subscript 0 denotes the values of the respective lengths at the beginning of stretch, *i.e.*, $t = 0$. As the plates separate, the mid-plane diameter decreases. From the time evolution of these two lengths, we can define two strain rates - the radial (true) strain rate and the axial (nominal) strain rate:

$$\dot{\varepsilon}_L \equiv \frac{1}{L}\frac{dL}{dt} \tag{2.7a}$$

$$\dot{\varepsilon}_D \equiv -\frac{2}{D_{mid}}\frac{dD_{mid}}{dt} \tag{2.7b}$$

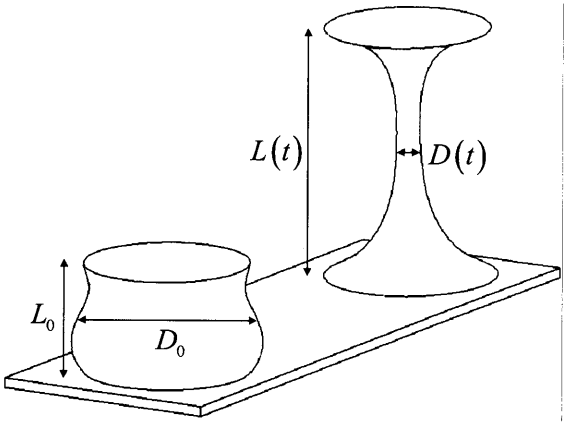

Figure 2–2: The endplate separation, L, and mid-plane diameter, D, of a fluid sample being stretched.

Once we have the strain rates, we can integrate them over time to get the total strains, or what is often called Hencky strain.

$$\varepsilon_D = \int_0^t \dot{\varepsilon}_D dt' = 2 \ln \frac{D_0}{D_{mid}} \tag{2.8a}$$

$$\varepsilon_L = \int_0^t \dot{\varepsilon}_L dt' = \ln \frac{L}{L_0} \tag{2.8b}$$

The Hencky strain in the axial direction takes the same form as the typical true strain defined in traditional solid mechanics. The radial strain is slightly different in that the initial diameter is in the numerator of the logarithmic function. This is because the radius decreases throughout the course of the stretching experiment, but we want the strain to be positive. The factor of 2 is present so that when the flow approaches the uniform elongational flow (UEF) limit, *i.e.*, a cylinder being stretched, the two strain rates are equal.

We can imagine two limits of the filament stretching kinematics. For the early parts of stretching, *i.e.*, small strains, the polymer has not been stretched enough to have any impact on the fluid deformation, so the flow can be considered to be a reverse squeeze flow with the solvent as the fluid. This comes from lubrication theory performed with Newtonian fluid mechanics since the solvent is Newtonian. At larger strains, strain-hardening changes the way the fluid deforms. The deformation is very close to being an uniform elongation flow. The fluid far away from the endplates can be treated and modelled as a one-dimensional flow, as the axial velocity becomes fairly independent of the radial distance [37, 36]. Thus, we have a relationship between the two strain rates for our two limits:

$$\text{lubrication}: \ \dot{\varepsilon}_D = \frac{3}{2}\dot{\varepsilon}_L \tag{2.9a}$$

$$\text{UEF}: \ \dot{\varepsilon}_D = \dot{\varepsilon}_L \tag{2.9b}$$

From the two strains, we can construct a master curve. The master curve shows the relationship between the radial (true) strain and the axial (nominal) strain. Figure 2–3 shows a master curve for some typical filament stretching experiments. We

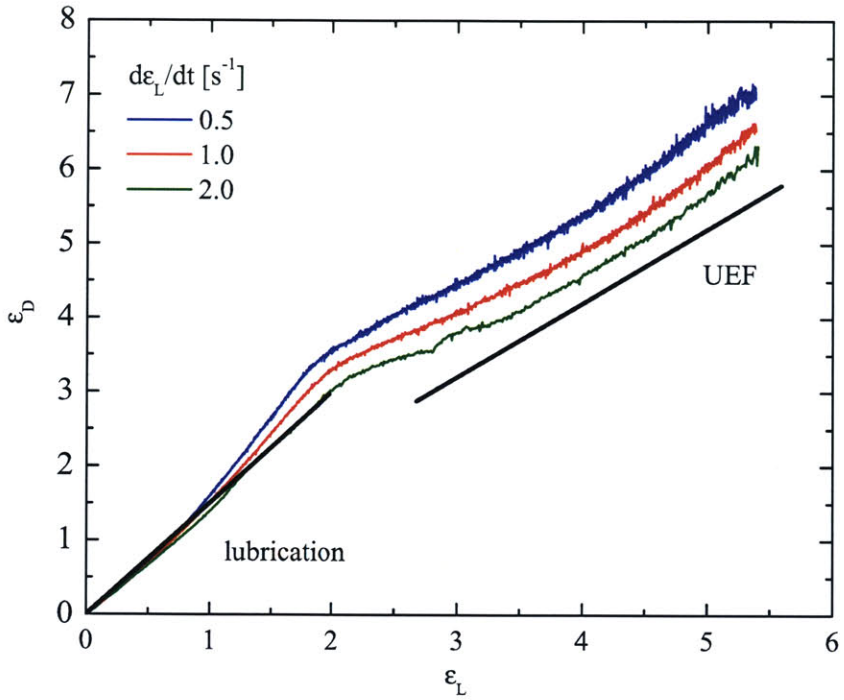

Figure 2–3: The master curve for a filament stretching experiment.

see that the master curve depends very much on strain rate. For lower rates, the fluid breaks "faster," *i.e.*, the amount of axial strain necessary to reach a certain radial strain is lower. For the rates shown, the master curve follows the limit given by lubrication theory for strains up to $\varepsilon_L \sim 1.5$. It starts to follow the uniform elongational flow limit at around $\varepsilon_L \sim 3.5$.

2.2.2 Dynamics

We now consider the dynamics of a fluid sample being stretched. We first define the stress tensor:

$$\pi = p\delta + \tau = \begin{pmatrix} p+\tau_{rr} & 0 & 0 \\ 0 & p+\tau_{\theta\theta} & 0 \\ 0 & 0 & p+\tau_{zz} \end{pmatrix} \tag{2.10}$$

π is stress from the hydrostatic pressure. The fluid stress is purely diagonal because the flow is shear-free. We can avoid dealing with stress associated with the hydrostatic pressure by taking the normal stress difference:

$$\langle \pi_{zz} - \pi_{rr} \rangle = \langle \tau_{zz} - \tau_{rr} \rangle \tag{2.11}$$

The force balance that allows us to determine the normal stress difference will be given later in section 3.2. From here, we can define the extensional viscosity:

$$\langle \tau_{zz} - \tau_{rr} \rangle = \bar{\eta}_E \dot{\varepsilon} \tag{2.12}$$

The extensional viscosity is the material property we are after in our study. We would like to measure the steady state value as well as the transient behavior of extensional viscosity. For more in-depth discussions of material properties, see [43] and [26].

2.3 Kinetic Theory of Visco-elastic fluids

Up until now, we have only defined values - geometrically, kinematically, and dynamically - that hold for all fluids in extensional flow. We now consider the effects of a polymer chain in a Newtonian solvent. A good overview of the kinetic theory of polymer solutions can be found in Larson's review of dilute polymer solutions [19].

2.3.1 Coarse Graining

When considering a long polymer chain, we can not possibly look at every single carbon and hydrogen atom. If we take each carbon-carbon chain to represent a freely rotating link, we can then simplify segments of the chain into a link of the Kramer bead-rod chain. We can then further simplify each bead-rod chain into segments of a bead-spring chain. See figure 2–4. In each simplification, called coarse-graining, we reduce the level of complexity of the polymer chain. This is important if we want to simulate polymer behavior during various deformations. The goal is to pick

the appropriate amount of coarse-graining that will give the best results while being simple (computationally inexpensive) enough to compute on a personal computer.

2.3.2 Bead-rod and Bead-spring Models

As shown in figure 2–4, we can represent a freely-rotating chain of molecules as a rod in the bead-rod model. These rods, each representing a Kuhn step, are freely-jointed and follow a conformation that is governed by random walks. The number of rods in a bead-rod model grows with the molecular weight. Current computational capabilities can only handle polymers with a few hundred rods. The computation is expensive not only because of the large number of rods, but also because the time steps required is very small, as the rods move very rapidly. For the polystyrene we use, which has a molecular weight of $M_w \approx 2.25 \times 10^6$ g/mol, the number of rods in the bead-rod model exceeds 1000, making the computational costs too high. Therefore, we coarse-grain multiple bead-rod sections into a spring, resulting in the bead-spring chain.

In the bead-spring model, the spring represents entropic elasticity. This is the effective spring force that is pulling the two ends of the subchain (a chain of N_s rods) as the rods are in motion. The beads provide the viscous drag from the solvent on the polymer chains. Since the beads are of a constant radius, the viscous drag will remain constant. To account for the change in viscous drag as polymer chains are stretched and become oriented differently, the springs can be made non-linear to compensate for such changes.

Other forces to consider are hydrodynamic interactions (HI), excluded volume (EV) interactions, Brownian forces, internal viscosity (IV), and self-entanglement (SE). Hydrodynamic interactions arise when polymer chains influence each other or itself as they are deformed. In the case of our solutions, which are very dilute, HI comes from polymer chains interacting with itself.

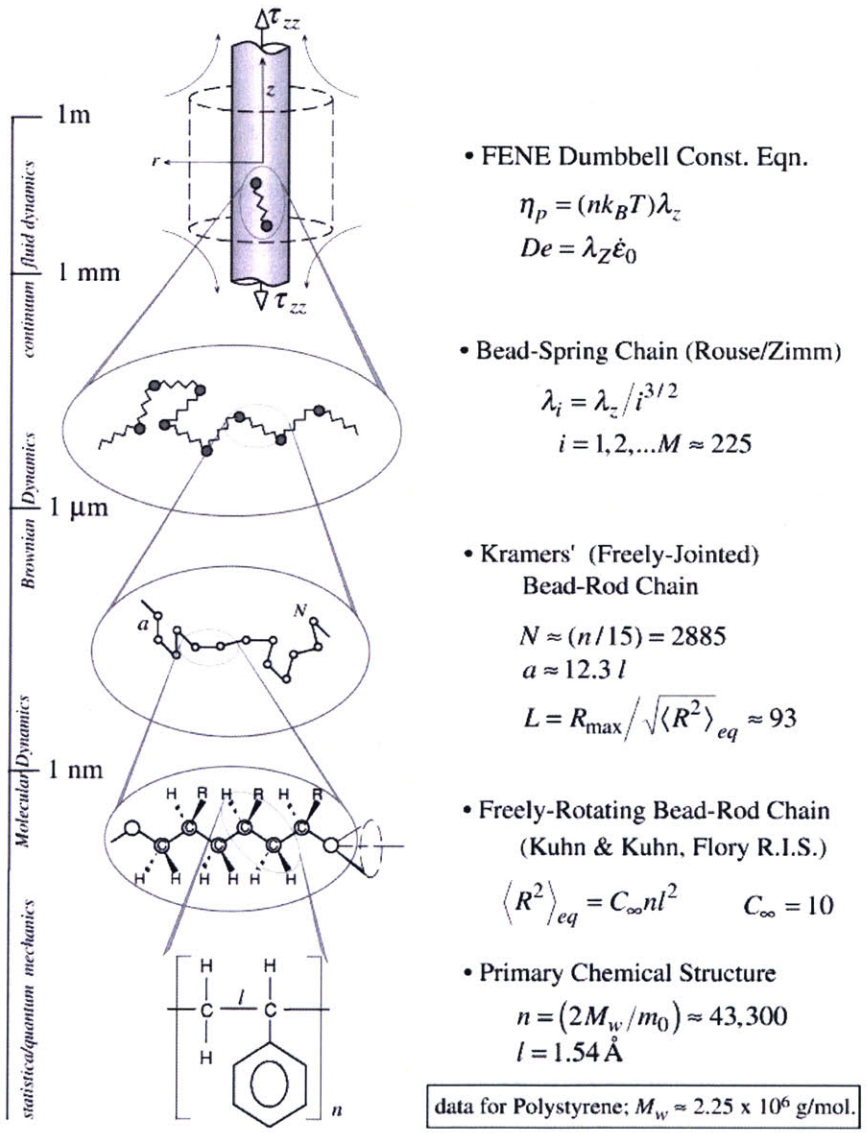

Figure 2–4: The various levels of coarse-graining in polystyrene with molecular weight $M_w \approx 2.25 \times 10^6$ g/mol. Taken from [26].

2.3.3 Rouse Model

To ensure that we have chosen the right level of coarse-graining, we check the relaxation times that the bead-spring chains experience. Since there can be a spectrum times, we notate them as λ_i, where the index i indicates the mode number. We first introduce the Rouse model as the simplest bead-spring model. It neglects both HI and EV and uses Hookean springs.

We take the viscous drag on the bead as given by Stoke's flow, where the drag coefficient, ζ, is given by $\zeta = 6\pi\eta_s a$. Here, η_s is the solvent viscosity and a is the bead radius. The total drag of the coil is then $\zeta_{coil} \equiv \zeta N$. Skipping the details of derivation, we can represent the relaxation times of the i^{th} mode as:

$$\lambda_i \approx \frac{\zeta_{coil} \langle R^2 \rangle_0}{6\pi^2 k_B T i^2} \propto \frac{1}{i^2} \tag{2.13}$$

The longest relaxation time has been show experimentally to be related to the intrinsic viscosity, $[\eta]$, by:

$$\lambda_{longest,R} = \frac{[\eta]\,\eta_s M_w}{S_1 N_A k_B T} \tag{2.14}$$

where S_1 is a factor representing the distribution of relaxation times.

$$S_1 = \frac{\sum \lambda_i}{\lambda_1} \tag{2.15}$$

For the Rouse model, *i.e.,* equation 2.13, $S_1 = \pi^2/6 = 1.645$. The relaxation strength, G_i, is the same for all modes, *i.e.,* $G_i = G$, and is given by:

$$G_i = G = nk_B T = \frac{cN_A k_B T}{M_w} \tag{2.16}$$

From this, we can express as storage and loss moduli as:

$$G'(\omega) = \sum_i \frac{G_i (\lambda_i \omega)^2}{1 + (\lambda_i \omega)^2} = \frac{cN_A k_B T}{M_w} \sum_i^{N_m} \frac{(\lambda_i \omega)^2}{1 + (\lambda_i \omega)^2} \tag{2.17a}$$

$$G''(\omega) = \frac{cN_A k_B T}{M_w} \sum_i^{N_m} \frac{\lambda_i \omega}{1 + (\lambda_i \omega)^2} \tag{2.17b}$$

2.3.4 Zimm model

The Zimm model takes the Rouse model and includes hydrodynamic interactions. As opposed to equation 2.13, where the the relaxation time of the i^{th} mode scales with $1/i^2$, the relaxation times are now given by:

$$\lambda_i = \frac{\lambda_1}{i^{2+\sigma}} \tag{2.18}$$

with the longest relaxation time now given by:

$$\lambda_{longest,Z} = \frac{1}{\zeta(3\nu)} \frac{[\eta] \eta_s M_w}{N_A k_B T} \tag{2.19}$$

ζ is the Riemann zeta function, given by:

$$\zeta(3\nu) = \sum_{i=1}^{\infty} \frac{1}{i^{3\nu}} \tag{2.20}$$

σ is given by:

$$\sigma \approx -1.4 (h^*)^{0.78} \tag{2.21}$$

h^* is a parameter that represents the degree of hydrodynamic interaction, with $h^* \approx 0.25$ for a theta solvent.[1] Taking the value of h^* for a theta solvent, we get that the relaxation times scales as $\lambda_i \propto 1/i^{1.525}$.[2] From this, we can again express the storage and loss moduli as a sum of relaxation times and strength. The expression is very

[1] $h^* \approx 0.25$ was the "special" value that Bird *et al.* noted in [7]. It is calculated to be $h^* = 0.267$ for the Zimm model using the Flory-Fox parameter for theta solvents [19].

[2] Zimm originally had the scaling as $\lambda_i \propto 1/i^{3/2}$, whose exponent is very close to the 1.525 given.

similar to equation 2.17, but with some additional terms as the mode number i is more involved in the summation:

$$G' = \frac{cN_AkT}{M_w}\sum_{i}^{N_m}\frac{(\lambda_z\omega)^2}{i^{2(2+\sigma)}+(\lambda_z\omega)^2} \tag{2.22a}$$

$$G'' = \eta_s\omega + \frac{cN_AkT}{M_w}\sum_{i}^{N_m}\frac{\lambda_z\omega i^{2+\sigma}}{i^{2(2+\sigma)}+(\lambda_z\omega)^2} \tag{2.22b}$$

In general, experimental data for linear viscoelastic material functions, G' and G'', have good agreement with the Zimm theory when the solution is dilute. See section 5.2.1 for comparison of the Zimm theory with experimental data.

2.4 FENE Models

Rheological behavior is often modeled with the FENE-P (Peterlin approximation) dumbbell. This model falls in the most coarse-grained level in figure 2–4. This model, however, does not capture the spectrum of relaxation times that is found in polymeric solutions. The FENE-P chain model can be used to capture the contributions from other relaxation times, but at a heavy cost because of the large number of coupled equations. To model a FENE-P chain with N modes, the number of equations scales with N^2. Wedgewood [51] proposed the FENE-PM model that uses decoupled equations. It produces rheological behaviors similar to the FENE-P chain, but at a much lower cost. The calculations required only scale with N. In the following sections, we take a look at how adding more modes to the FENE-PM model affects the stresses, and hence extensional viscosity, in elongational flows. We also try to determine how many modes is required to get a "good" approximation for the stress contribution from the polymer.

2.4.1 FENE-PM

Entov and Hinch study a FENE model with multiple modes in [14], with each mode experiencing a deformation $A_i(t)$. In elongational flow, axial symmetry allows the deformation to be broken down into $A_{zz,i}(t)$ and $A_{rr,i}(t)$. These deformations behave according to:

$$\dot{A}_z^i = 2\dot{\varepsilon}A_z^i - 1\frac{1}{\lambda_i}\left(fA_z^i - 1\right) \tag{2.23a}$$

$$\dot{A}_r^i = -\dot{\varepsilon}A_r^i - 1\frac{1}{\lambda_i}\left(fA_r^i - 1\right) \tag{2.23b}$$

where $\dot{\varepsilon}$ is the strain rate, λ_i is the relaxation time of the ith mode. We saw in equation 2.18 that the relaxation time spectrum of the Zimm model scales as $\lambda_i \propto \frac{1}{i^{2+\sigma}}$, with σ being a measure of hydrodynamic interactions. Finally, f is a FENE factor determined by:

$$f = \frac{1}{1 - \frac{1}{L^2}\sum_{i=1}^{N} A_i} \tag{2.24}$$

L^2 is the measure of finite extensibility of the modes, which is the same for all modes.[3] This allows us to compute the stress as:

$$\tau_p = (nk_BT)\, f \sum_{i=1}^{N} \left(A_{zz,i} - A_{rr,i}\right) \tag{2.25}$$

The p subscript denotes stress from the polymer. Total stress can then be calculated from $\tau = \tau_p + \tau_s$, where $\tau_s = 3\eta_s\dot{\varepsilon}$ is the stress contribution from the solvent.

2.4.2 FENE-PM Simulations

With the equations in 2.23, the deformation can be solved with *Matlab*'s ODE solver. For the following simulations, the material properties used are that of PS025, with

[3] It is calculated from $L^2 = 3\left(\frac{j\times 0.816^2}{m_0 C_\infty}\right)^{2(1-\nu)} M_w^{2(1-\nu)}$.

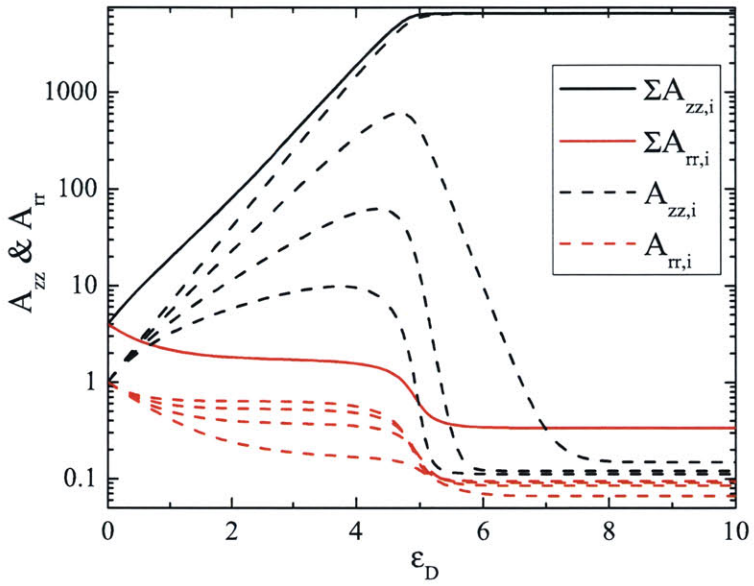

Figure 2–5: FENE-PM for a strain rate of $\dot{\varepsilon} = 1\ \mathrm{s}^{-1}$. The deformation components, $A_{zz,i}$ and $A_{rr,i}$, for each mode (four total), as well as the sum of all the modes.

longest relaxation time $\lambda_1 = 5.02\mathrm{s}$, performed at a temperature of $T = 25°\mathrm{C}$. Other relevant properties can be found in table 5.1.

Figure 2–5 shows FENE-PM with four modes under a strain rate of $\dot{\varepsilon} = 1\ \mathrm{s}^{-1}$. The deformation components $A_{zz,i}$ and $A_{rr,i}$ are plotted for each mode, as well as the sum of all the modes. The first mode sets the steady state value. Subsequent modes add negligible amounts to the steady state value. From the second mode and onwards, the only contribution is towards the transient response.

Figure 2–6 shows the polymer stress, τ_p, for the same strain rate with increasing number of modes. As the figure shows, the addition of each mode has a less and less effect. By the fourth or fifth mode, the stress is very close to what seems like a converging curve. Figure 2–7 shows the total stress, which is the sum of the polymer and solvent stresses.

As expected, $A_{zz,i}$ grows to some value, then becomes limited by the FENE parameter, f, as the polymer reaches its maximum extension. The first mode reaches a steady state while the others drop. At the first mode, the FENE parameter is just

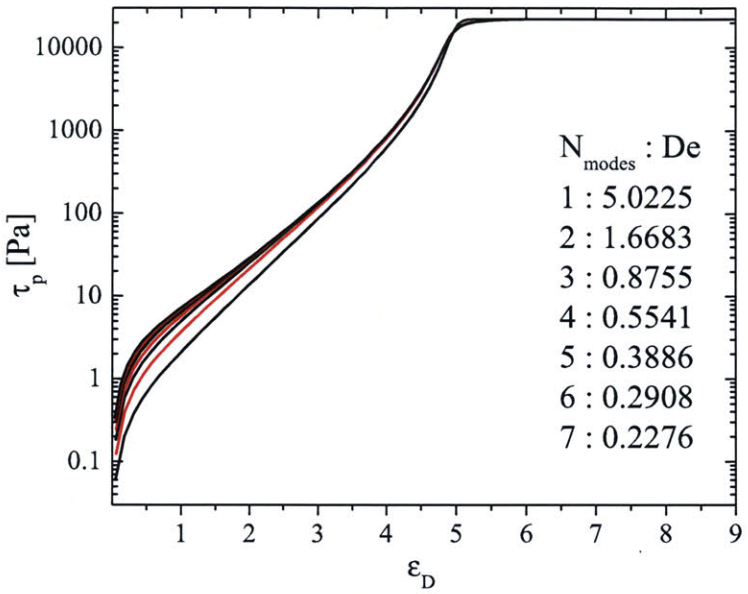

Figure 2–6: The effect of changing the number of modes used in the FENE-PM model on the total polymer stress. The strain rate is $\dot{\varepsilon} = 1\ s^{-1}$. Each line represents the total polymer stress with the corresponding number of modes that was used. Additional modes increase the total polymer stress.

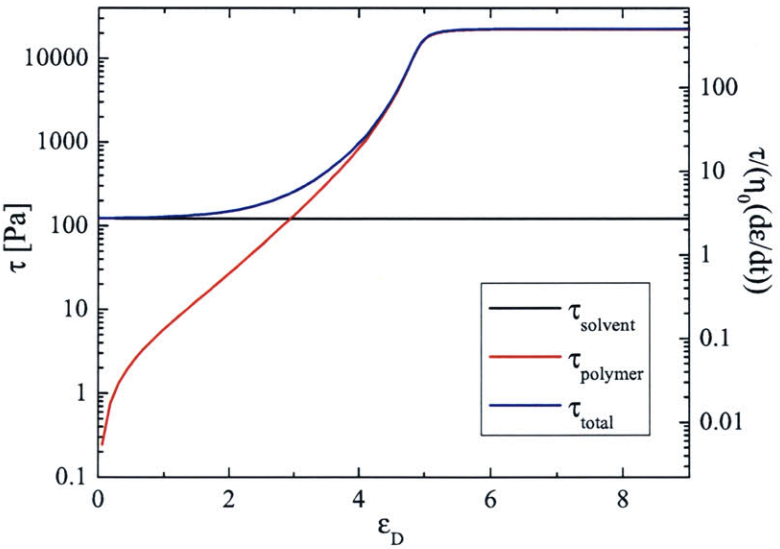

Figure 2–7: Total fluid stress, as predicted by FENE-PM. Both solvent and polymer contribute to the total stress. The strain rate is $\dot{\varepsilon} = 1\ s^{-1}$.

at the right size that keeps A_{zz} at the finite length. However, because the FENE parameter is the same for all modes, it actually reduces A_{zz} for the other modes. On the other hand, $A_{rr,i}$ decreases to some steady value.

It is helpful to find a way to determine how many modes are sufficient to model the transient response. We refer to studies on elongational flow with varying De numbers (in the case with no finite extensibility). At high De numbers ($De > 1$), the polymer is pulled so fast that it does not have time to relax. As a result, the stress increases exponentially. At $De = 1$, the stress increases at the same rate as the area is decreasing, so the force reaches a constant. For $\frac{1}{2} < De < 1$, the area decreases faster than the stress, so the resulting force experiences a maximum. The stress still increases exponentially, but not as rapidly as before. At $De = \frac{1}{2}$, the flow is stretching the polymer just at the rate so that that polymer increases only linearly. At $De < \frac{1}{2}$, the polymer has time to relax. The flow keeps the polymer stretched at a finite length so that the stress reaches a constant.

The analysis above can be used with FENE-PM models. Each mode will have a slightly different De number, as the relaxation times are different for each mode. De decreases with each mode. Instead of increasing forever, the stress now has a maximum limit because the polymers can only be stretched to a finite length. Polymers experiencing $De > \frac{1}{2}$ will give significantly higher stress contributions than polymers experiencing $De < \frac{1}{2}$.

To demonstrate the effects of varying De numbers, figure 2–8 shows a polymer experiencing a strain rate such that the largest De number is less than $\frac{1}{2}$. Note that the stress contribution from the polymer is so low that is dominated by the solvent contribution.

Conversely, if the De is high, then the number of modes needed is increased. Figure below shows a strain rate of 5 s^{-1}, so that the longest relaxation time is $\lambda_1 = 25.1$ s. The De number does not decrease below $\frac{1}{2}$ until the 14th mode. As a result, each mode show actually adds a significant amount to the total transient stress response - *i.e.,* the two outer-most curves.

Finally, we show what FENE-PM predicts for the extensional viscosity, η_E. We

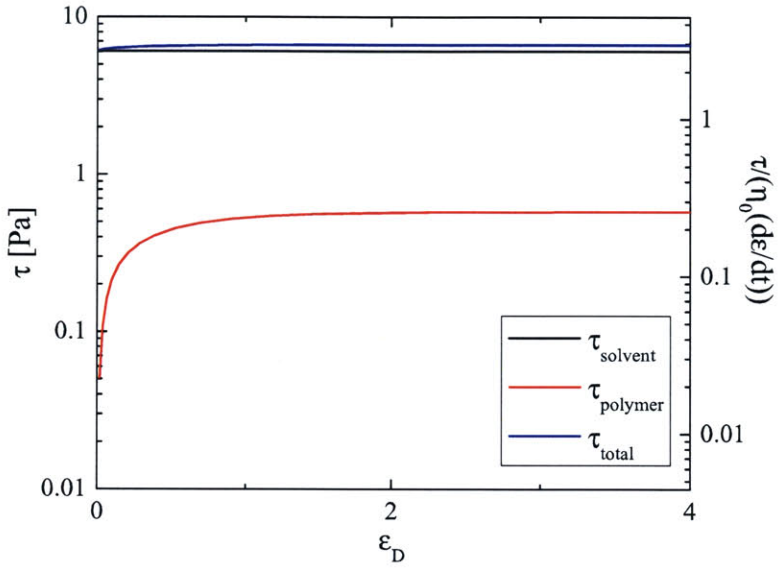

Figure 2–8: Total fluid stress resulting from a stretching experiment with a low strain rate. Here, the strain rate is $\dot{\varepsilon} = 0.05\ \mathrm{s}^{-1}$, giving a Deborah number of $De = 0.25$. The solvent stress dominates the polymer stress.

define this in greater detail in the next chapter. Figure 2–9 shows the transient extensional viscosity for a series of strain rates ranging from $\dot{\varepsilon} = 0.1 - 100\ \mathrm{s}^{-1}$. Figure 2–10 shows the steady state extensional viscosity as a function of strain rates or Deborah number, De. As mentioned above, the extensional viscosity is dominated by the solvent stresses, $\eta_E = 3\eta_s$, for low De flows. The polymer stresses do not contribute until De approaches $\frac{1}{2}$. Above the critical $\frac{1}{2}$ value, the extensional viscosity reaches a limiting value set by the length of the polymer chains.

2.4.3 Comments on FENE-PM

In section 2.4.1, we introduced the FENE-PM model. The FENE-PM is in essence a Rouse chain whose linear springs has been replaced by a FENE springs. Gupta *et al.* [16] measured the extensional viscosity of dilute polystyrene solutions with varying strain rates. His studies showed the results in comparison with FENE-PM and also FENE-P with the Zimm relaxation spectrum (obtained from shear rheological data). The FENE-P with Zimm parameters was not able to accurately capture the growth

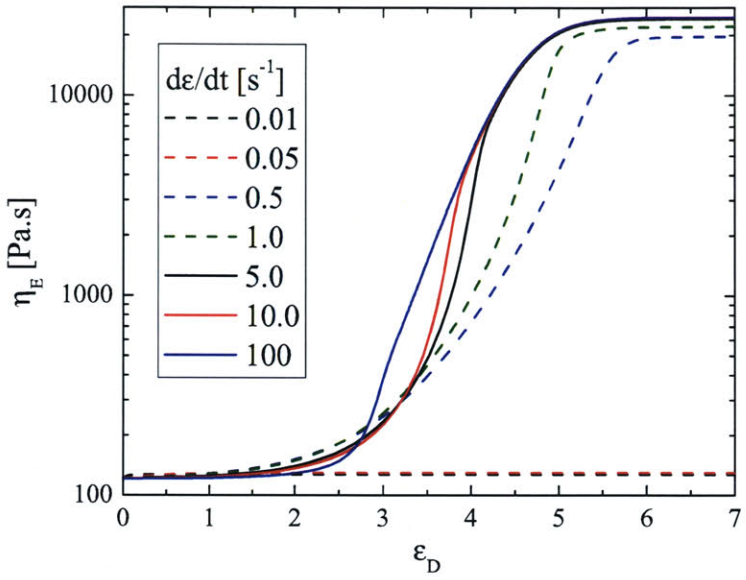

Figure 2–9: Extensional viscosity as predicted by FENE-PM, for a range of strain rates. For low rates, the Deborah number is sufficiently low such that the extensional viscosity is solely determined by the solvent, resulting in a flat line.

of extensional viscosity. The stretching causes the drag on the chains to behave more like a Rouse chain, *i.e.,* it experiences very little hydrodynamic interactions. ...

2.5 Dimensionless Groups

To measure the fluid stresses, we use a force transducer as the bottom endplate. The specifications of this force transducer will be given in section 3.1.3. There are many forces that contribute to the total force being measured. A detailed force balance will be discussed in detail in section 3.2. Besides the forces that come from the fluid stress, we also need to consider viscous, inertial, gravitational, and surface tension effects. To get a get a good sense of the various degrees of magnitudes, it is useful to define dimensionless numbers to compare the different contributions.

The Reynolds number, Re, is the ratio of inertial to viscous effects. A low Re means that we can neglect the inertial

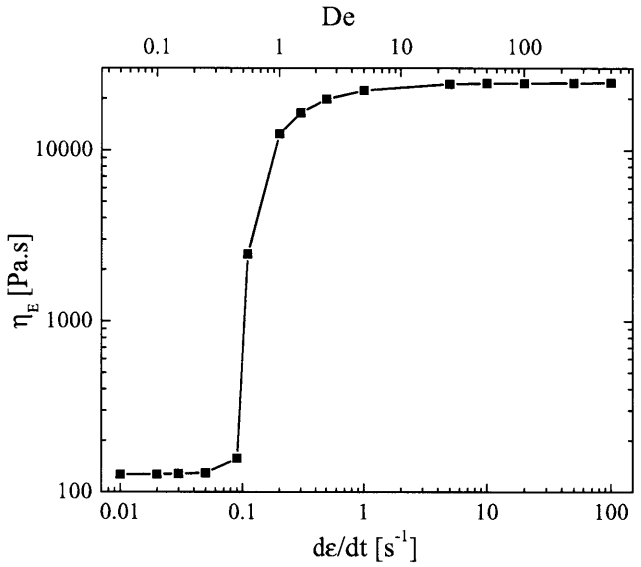

Figure 2–10: Steady state extensional viscosity, as predicted by FENE-PM, as a function of strain rate. The x-axis can be represented as strain rate, bottom axis, or Deborah number, top axis. The jump from solvent dominated stresses to polymer dominated stresses occurs at $De = \frac{1}{2}$.

$$Re = \frac{\text{inertia}}{\text{viscous effects}} = \frac{\rho\dot{\varepsilon}L_0^2}{\eta_0} = 3.4 \times 10^{-4}\dot{\varepsilon} \tag{2.26}$$

The Bond number, Bo, is the ratio of gravitational to surface tension effects. A low Bo tells us that we can neglect gravitational effects.

$$Bo = \frac{\text{gravity}}{\text{surface tension}} = \frac{\rho g D_0^2}{4\sigma} = 0.81 \tag{2.27}$$

The capillary number, Ca, is the ratio of viscous to surface tension effects.

$$Ca = \frac{\text{viscous effects}}{\text{surface tension}} = \frac{\eta_0\dot{\varepsilon}D_0}{\sigma} = 2.25\dot{\varepsilon} \tag{2.28}$$

The ratio of the Bond number to the Capillary number represents the ratio of gravitational to viscous effects.

$$\frac{Bo}{Ca} = \frac{\text{gravity}}{\text{viscous effects}} = \frac{\rho g D_0}{4\eta_0\dot{\varepsilon}} = \frac{0.36}{\dot{\varepsilon}} \tag{2.29}$$

Finally, the Deborah number, De, is the ratio of the material time scale to the experimental time scale.

$$De = \frac{\text{material time scale}}{\text{experimental time scale}} = \lambda\dot{\varepsilon} = 5\dot{\varepsilon} \tag{2.30}$$

The material time scale used in our expression is the relaxation time, λ, of the polymer solution. The experimental time scale has to do with how fast we are exciting the polymers in the solution, namely the strain rate. As $De \rightarrow 0$, *i.e.,* the imposed flow is so slow that the polymers are never excited, we reach the Newtonian fluid limit. As $De >> 1$, we reach the elastic solid limit.

Chapter 3

Filament Stretching

There are different ways to study the extensional rheology of liquids. We will first go over the instrumentation of the experiment, detailing the hardware components that are used in stretching the fluids and measuring the quantities necessary for extensional rheology. We will quickly review the kinematics that was discussed in section 2.2.1 and show how that affects the various stretching experiments.

3.1 Hardware

The filament stretching extension rheometer (FiSER) used in our study consists of a DC linear motor, a laser micrometer, and a force transducer. A schematic of the filament stretching extensional rheometer (FiSER) is shown in figure 3–1. A summary of the hardware specifications is given in table 3.1. We now discuss each component in detail.

3.1.1 Linear Motor

The linear motor, made by NorMag (Northern Magnetics, Inc.,[1] model EPS-1200), is capable of reaching extensions of 2 m and speeds of 5 m/s. There are two motors on the stage. The top motor carries the top endplate, which in turn stretches the fluid.

[1]NorMag has been acquired by Baldor.

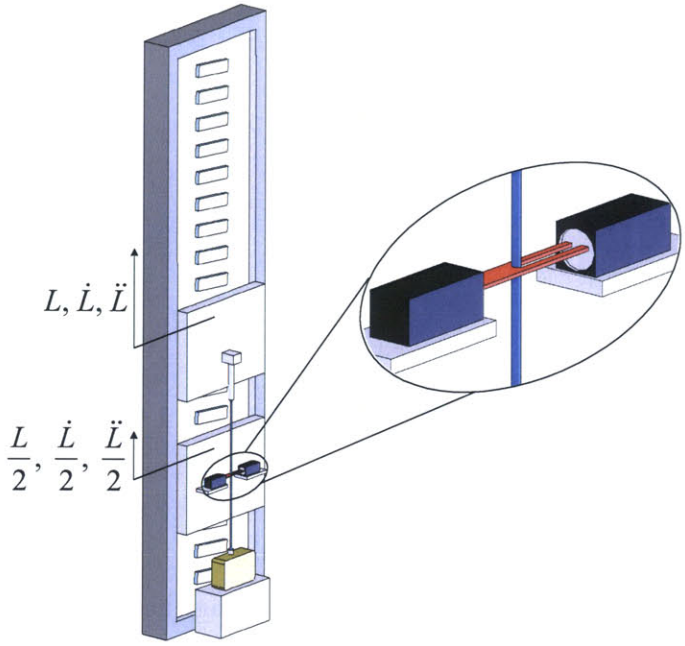

Figure 3–1: Schematic of the filament stretching extensional rheometer (FiSER).

The bottom motor carries the laser micrometer, which measures the diameter of the fluid sample. The bottom endplate is the force transducer, which stays stationary. The laser micrometers always stays at the half-way point between the top and bottom endplates. Thus, the bottom motor will always travel at half the position, velocity, and acceleration as the top motor. This allows us to measure the mid-plane diameter of the fluid sample.

The motors are driven by the Delta Tau Programmable Multi-Axis Controller (PMAC). The signals from the PMAC are sent through two amplifiers (Glentek SMA8315-1A-1), which then feed the amplified signals and power to the motors. Variables and programs are downloaded from and uploaded to a personal computer (PC, Dell Dimension 8200) through the Delta Tau software interface (PeWin 32 Pro) via a RS-232 (serial port) connection. Force and diameter measurements are made through the Delta Tau 16-bit A/D DAQ accessory board (ACC-28B). While the motion programs are running, all calculations and communication are done within the PMAC and the motors, and not involving the computer (PC). The PC is only used

Table 3.1: *FiSER hardware specifications.*

Motion	
L_{max}	1.5 m
$\Delta L_{min,controllable}$	150 μm
$\Delta L_{min,observable}$	1 μm
V_{max}	2 m/s
Diameter Measurement	
D_{max}	9 mm
D_{min}	50 μm
ΔD_{min}*	10 μm
Force Measurement	
F_{max}	$\pm$10 g
ΔF_{min}	0.01 g

* Refers to resolution, which is different from the smallest measureable diameter, D_{min}.

to write the programs, send the programs to the PMAC before an experiment, and retrieve the data from the DAQ board after the experiment.

Motion programs are written in a proprietary language specific to Delta Tau controllers. The Delta Tau PMAC runs on an internal clock with 447 μs cycle time. Data can be captured at time intervals that are multiples of this cycle time.

There have been other filament stretching rheometers built with different linear motors. Linear motors have different specifications based on manufacturer and model. Furthermore, linear motors are usually paired with specific controllers,[2] and different controllers have different capabilities in terms of calculating trajectories for motion blending. For a list and comparison of some of the other extensional rheometers, see [2].

3.1.2 Laser Micrometer

The laser micrometers are made by Omron (model ZL4A). It is capable of measuring diameters down to 50 μm with 5 μm resolution and has a response time of 0.5 ms. Figure 3–2 shows a typical calibration of the laser micrometers. The data points are acquired with various optical fibers and plastic rods, to simulate the transparency of

[2]In our setup, we have NorMag motors controlled by Delta Tau PMAC.

the fluid samples.[3] The minimum and maximum voltages are 1 and 5 V respectively.

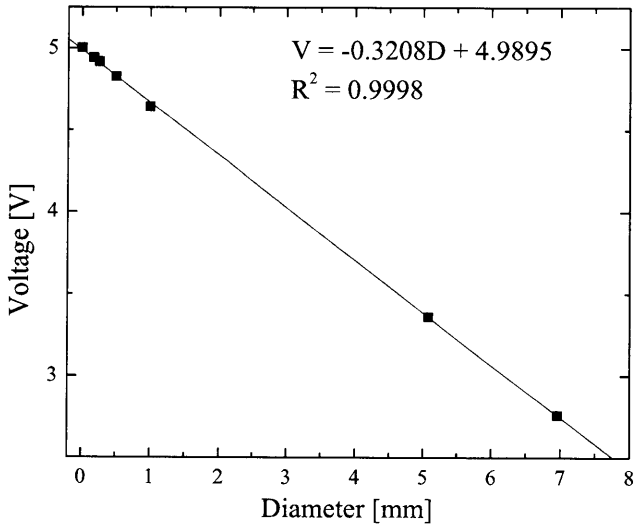

Figure 3–2: Calibration of the Omron laser micrometers.

3.1.3 Force Transducer

The force transducers are made by Futek (Q07512). It is used in conjunction with an amplifier (Futek JM3). The transducer can measure forces of ± 10 kdynes (*i.e.*, 10 kdyne in both tension and compression), and has a response time of 50 ms. Figure 3–3 shows a typical force calibration, done with Ohaus® weights.

We need to determine the dynamics of the force transducer before we can use it to calculate the stresses in the fluid sample. The transducer outputs a voltage to the data acquisition system (DAQ), and the values from the DAQ is then translated to a force measurement. There is complexity introduced by the dynamics, which tells us how the input relates to the output. We analyze the dynamics by creating a Bode plot of output response of the transducer. We excite the transducer at various frequencies by mounting a magnet on the transducer and holding it under an electromagnet, which is controlled with a lock-in amplifier (EG&G 7260). We can then measure the

[3]For opaque objects, the calibration changes noticeably, but still retains the linear behavior.

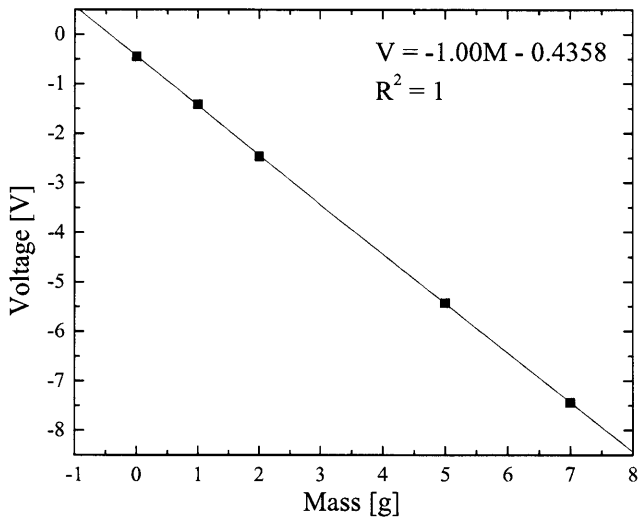

Figure 3–3: Calibration of the Futek force transducer. Ohaus weights were used to calibrate the transducer in compression. The linearity is preserved with forces in tension (results not shown here).

magnitude and phase response of the transducer. From these data, we generate a Bode plot, as shown in figure 3–4.

Once we have a Bode plot, we can try to model it to estimate what a typical response would be. This is done by fitting a linear system of poles and zeros that would result in a similar Bode plot. For the Bode plot given in figure 3–4, we approximated the system to have seven poles. Given these poles, we can simulate a step response of the system. Figure 3–5 shows a step response of the transducer along with the model prediction of the 7-pole system. To simulate a step input experimentally, a weight was placed on the transducer, and pulled off with a string. There is a bit of discrepancy in the initial responses. This is due to the human error introduced as the weight is pulled off manually. The important characteristic is the slope of the curve - a measure of the rise time[4] - as it rises from initial to final values.

The Bode plot of the transducer response tells us that for strain rates of up

[4]Rise time is typically defined as the amount of time needed for a signal to change from a specified low value to a specified high value in response to a step input. The specified low and high values are typically 10% and 90%, respectively.

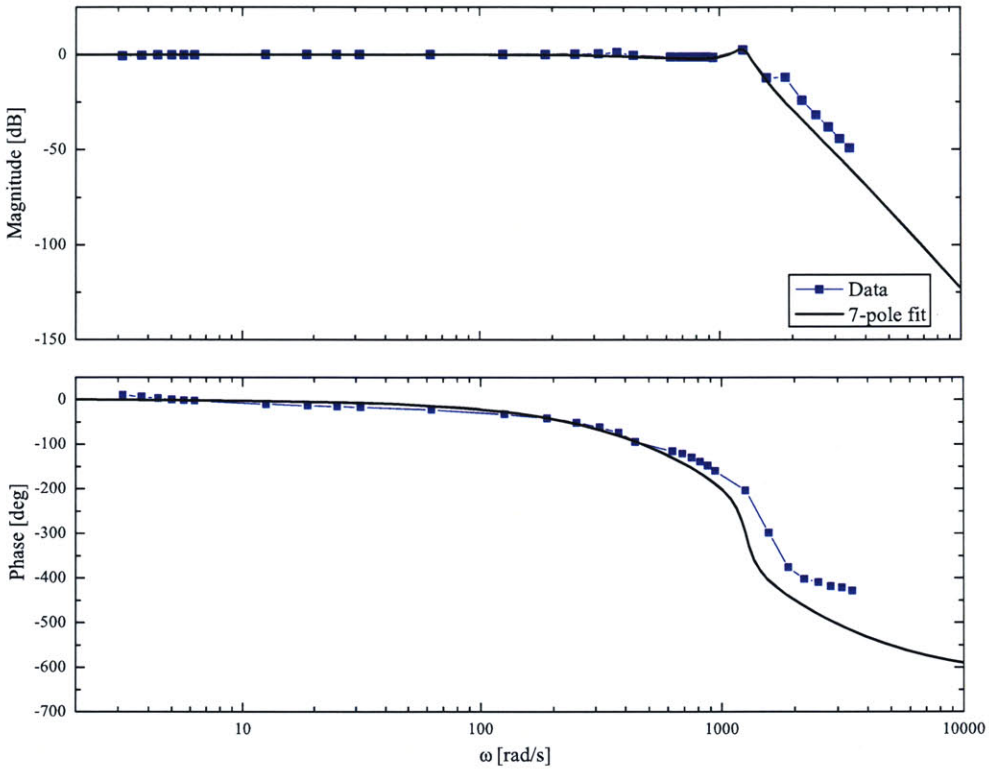

Figure 3–4: Bode plot of the Futek force transducer. The blue points are the data collected by inputting a sinusoidal signal with the EG&G lock-in amplifier and comparing it with the output from the transducer. The black line is the 7-pole linear system that was fit to the data.

to $\dot{\varepsilon} = 1260\ \mathrm{s}^{-1}$, the transducer will theoretically output the force input exactly. Since the maximum strain rates that the fluid samples are subjected to are orders of magnitudes smaller, we can safely use the raw voltage as a good estimation of the force measurement without having to de-convolute the signal. This is different from the case as presented in Anna's studies [2]. The force transducer used in Anna's studies had a drop-off frequency of about $126\ \mathrm{s}^{-1}$, about an order of magnitude lower. This means that the transducer's voltage output can lag by as much as 10 ms, depending on the strain rates.

Figure 3–6 shows typical force measurements from two different experiments. Two different rates are shown, the higher rate experiment ends more quickly because the

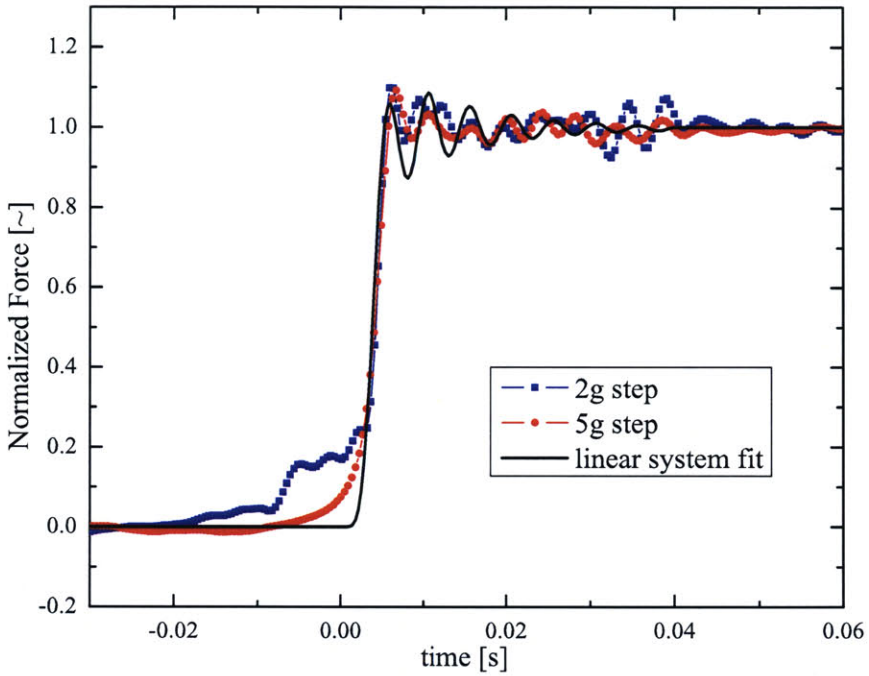

Figure 3–5: Step responses of the force transducer with two different steps. The forces have been normalized to be compared with the step simulation done in MatLab.

motors reach the maximum height faster. The force transducer is set close to zero voltage at initial times. Here, positive force corresponds to the transducer feeling a force in tension. As the fluid is stretched, the force "jumps" up to some higher value. The amount of time it takes for the transducer to jump to this higher value is related to the response time of the transducer. It then starts to drop just as a Newtonian fluid would. Then strain-hardening causes the force readings to rise, as the polymers are being stretched. The force readings are more pronounced in the higher rate experiment.

The Futek force transducer experiences noise electrically from the surrounding as well as vibrations from the motor motions. Figure 3–7 shows noise stemming from various sources. The reference reading is taken with all electrical components - motors, amplifiers - off. The data show noise can result from the electrical and mechanical noise. The electrical noise, which mainly come from the amplifiers, are significantly

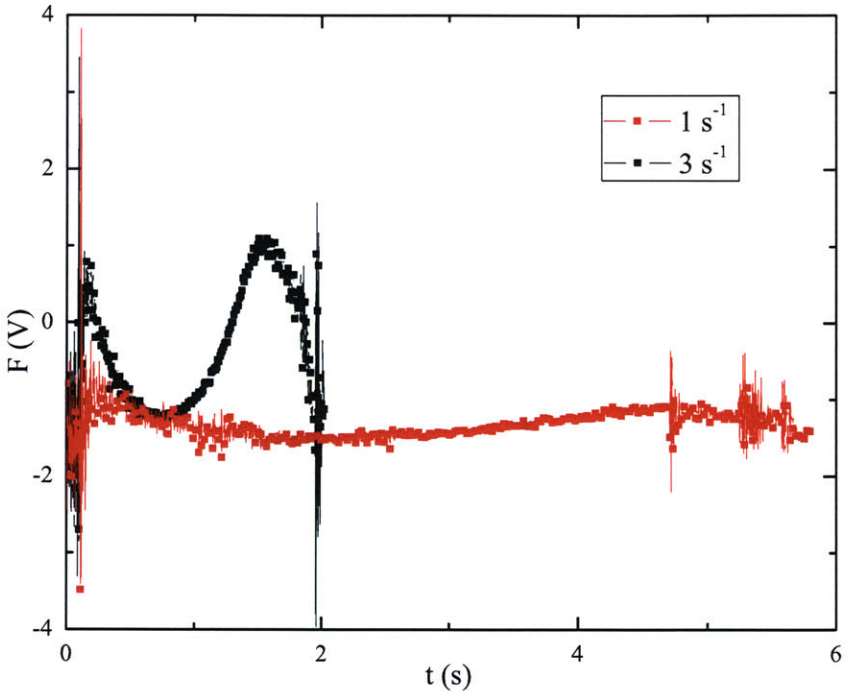

Figure 3–6: Typical force readings from a filament stretching experiment.

less than the mechanical noise, which comes from the vibration of the motors. Keep in mind that even when the motors are being asked to stay still, there are still small oscillations in position. This is because the motors are mounted vertically, and so force is constantly being generated to counter gravity.

3.2 Force Balance

To determine the forces that are acting on the fluid sample, we consider half the fluid sample. See figure 3–8. We assume that the fluid sample is symmetric about the mid-plane. The forces acting on this half sample control volume are the forces within the fluid, surface tension, inertia, gravity, and the force transducer, which exerts a force equal and opposite to the force that it measures. The magnitude comparison of these forces, done with dimensional analysis, is covered in section 2.5.

The force measured by the force transducer is really a sum of a number of forces.

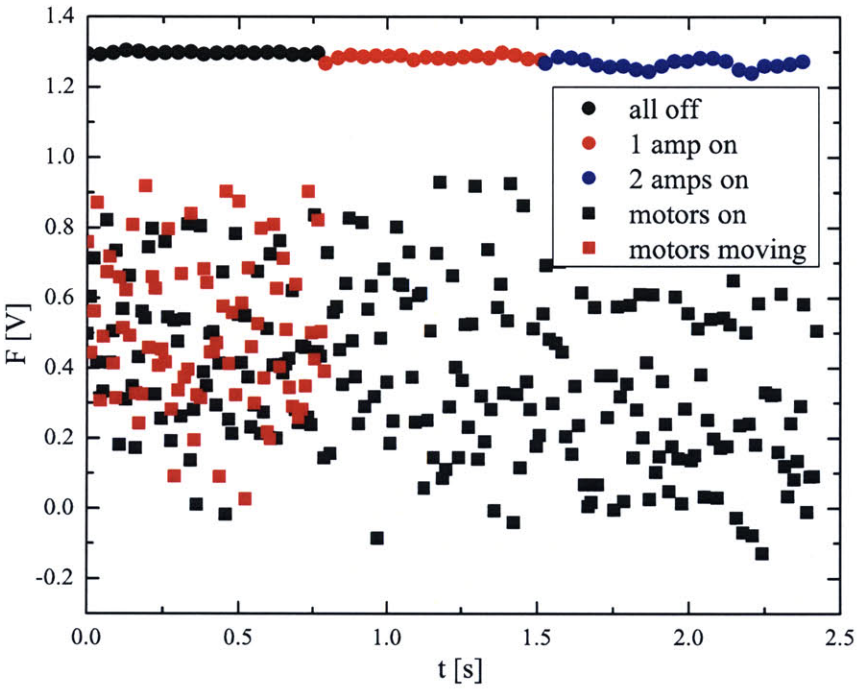

Figure 3–7: Noises in force measurements from various sources. For the data with motors moving, the motors were set to move exponentially apart.

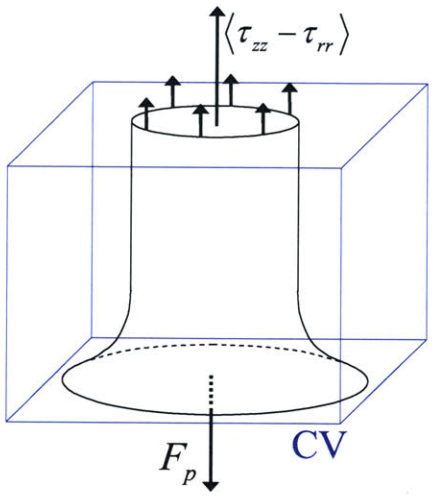

Figure 3–8: Force balance of a fluid sample cut at the midplane. The blue box marks the control volume.

To determine the fluid stress in the sample, we use the force balance given by Szabo [45]:

$$\langle \tau_{zz} - \tau_{rr} \rangle = \frac{F_p}{\pi R^2} + \frac{1}{2}\frac{\rho g V_0}{\pi R^2} + \left[\frac{\rho g \delta V}{\pi R^2}\right] - \frac{\sigma}{R} + \frac{1}{2}\frac{\rho V_0 \ddot{L}}{\pi R^2} \tag{3.1}$$

Equation 3.1 shows the various forces acting on the control volume. The term in the []'s, which includes δV, applies when the fluid sample is not completely symmetric about the midplane because of sagging effects. This occurs if the strain rates are low and the stress stemming from gravity becomes comparable to the fluid stress. δV is the extra volume of fluid that has entered the bottom half of the fluid sample. For our calculations, this term will be neglected. This term only becomes important for low strain rates and/or fluids with low viscosities. In such cases of low viscosity, δV is still often neglected because it is so difficult to measure. Video capture, and most likely video microscopy to get enough resolution to measure the fluid sample geometry accurately, is really the only way to measure the volume of the lower portion of the fluid.

Finally, from equation 2.12, we see that extensional viscosity is related to the fluid stress by $\langle \tau_{zz} - \tau_{rr} \rangle = \bar{\eta}_E \dot{\varepsilon} eqn : F_b al.$ We can non-dimensionalize the extensional

viscosity by scaling it with the zero-shear-rate viscosity, giving us the Trouton ratio, Tr:

$$Tr = \frac{\bar{\eta}_E^+}{\eta_0} = \frac{\langle \tau_{zz} - \tau_{rr} \rangle}{\eta_0 \dot{\epsilon}} \tag{3.2}$$

As we will see in the results, chapter 5, the Trouton ratio can span two to three orders of magnitude in the dilute polymer solution that we use. We have also seen hints of this from the simulations done with the FENE-PM model in section 2.4.2. This tells us that the polymer in solution can add significant amounts of stress. For processes such as plastic extrusion and fiber-spinning, this huge increase in stress is important to keep in mind when designing the machines that will be used.

3.3 Capillary Thinning and Break-up Experiments

We now discuss the different types of experiments in extensional rheology. Each type of experiment measures rheological properties in different ways. We present the experiments in the order of increasing complexity. In a capillary thinning experiment, the only motion required is a step function. In a stretch-to break experiment, the motion is very slow, and can hence be performed with simpler mechanical drive systems. In a filament stretching experiment, careful control of the motion is necessary.

To study capillary thinning and/or break-up of fluids, we apply a step strain to the fluid and measure its radius as it breaks up due to capillarity. Because this is the easiest experiment in terms of the strains imposed, a specific rheometer has been made to solely perform these type of experiments.

The capillary break-up extensional rheometer (CaBER) is made by the Cambridge Polymer Group (http://www.campoly.com). The CaBER consists of two 6 mm diameter endplates. The fluid sample is loaded between the two plates, which are initially set 2 to 3 mm apart. The top endplate then moves up vertically - the final separation can be adjusted from 8 mm to 15 mm. This imposes a step strain on the fluid. Where as the filament stretching rheometer (FiSER) can also perform a step strain, the CaBER uses a much simpler actuator, a solenoid, to impose the strain.

This allows the CaBER to be much smaller, run on much lower power, and be more easily controlled.

The setup is controlled by the CaBER software (version 3), written in Labview. Data acquisition is made with a National Instruments 1200 DAQ card. The maximum sampling rate is 1000 Hz. The mid-point diameter is measured with the same infrared laser micrometer as the FiSER (Omron Z4LA-D1030 beam transmitter with Z4LA-L10 beam sensor), discussed in section 3.1.2. The laser micrometer stays stationary throughout the experiment. The software calibrates the top endplate such that after it reaches its final height, the laser micrometer will be halfway between the top and bottom endplates.

CaBER uses capillarity as its means of measuring force - *i.e.,* it has its own built-in force transducer. The force inside the filament is balanced by surface tension, and this force can be calculated by measuring the mid-plane diameter.

CaBER is useful for studying the extensional rheology of dilute polymer solutions. The plate diameters and initial and final lengths can be adjusted for fluid samples with different surface tensions and viscosities. It also has the benefit of not requiring a force transducer as the capillary forces driving the process can be measured and used as the force measurement. The capillary forces are measured indirectly by monitoring the diameter of the fluid sample.

Figure 3–9 shows the position profile of the endplates and the master curve, see section 2.2 ,of a capillary break-up experiment. The experiment does not start until $t = 0$, when the step strain is imposed. The time it takes to reach the final height, or strain, is $\delta t = 50$ ms. The fluid used is PS025, which will be discussed in further detail in section 5.1.

3.4 Stretch-to-Break (STB) Experiments

In a stretch-to-break (STB) experiment, the fluid is stretched at a very low rate. The profile can either be linear (constant velocity, $L = L_0 + vt$) or an exponential ($L = L_0 e^{\dot{\varepsilon}t}$), with $\dot{\varepsilon} \ll 1$.

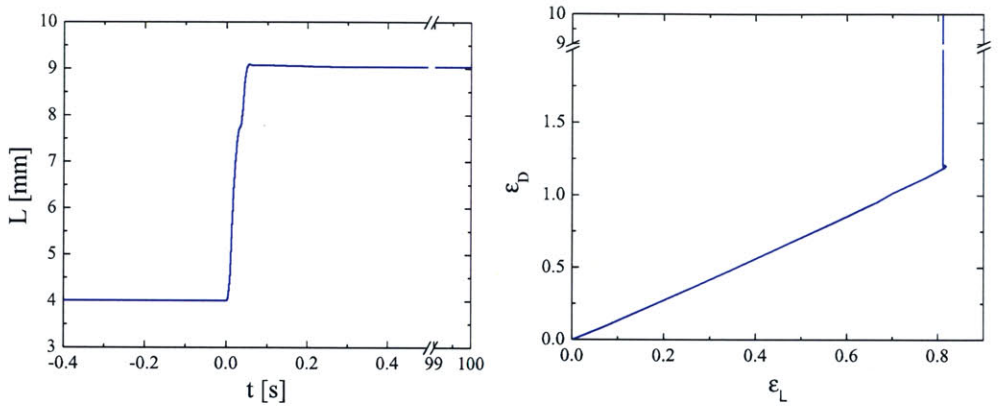

(a) position profile (b) master curve

Figure 3–9: A capillary break-up experiment, done with PS025. A step strain is imposed at $t = 0$, and the mid-plane radius is measured as the fluid breaks under capillarity.

Previous studies have called apparatus that do such experiments a "filancementer." We now present a few different versions of STB experiments that have been performed. The applications of these results are wide and many, as can be seen in the broad range of fields.

Burnett [11] and Chretien [13] used an "automatic device" that stretched mucus to test for spinnability. The device composed of a DC synchronous motor that lifts the top endplate through a rack and pinion set-up. This allowed the investigators to impose a constant velocity stretch. In a STB experiment, the fluid is being stretched so slowly that capillary forces act as the main mechanism of break-up, much like a CaBER experiment. Puchelle et al. [33] used the same device to study bronchial mucus. They noted a relationship between the spinnability, measured as the length that the fluid could be stretched, and mucous transport velocity.

Pitois [31] studied the rupture energy involved in a liquid bridge between two spheres. There sphere were separated at velocities in the range of $0.1 - 15$ μm/s. Analytical expressions for rupture energy associated with viscous and capillary effects were given. Pitois also noted that the distance to rupture increased with the separation velocity.

Yildirim [54] studied the breakup of stretching bridges of Newtonian liquids by stretching the fluid sample between two disks separated at constant velocities. They compared results to 1- and 2-dimensional models. 1-D models were able to predect macroscopic features of the breakup. They showed that the break-up of Newtonian and shear-thinning liquids is similar when the zero-shear viscosity or the Ohnesorge number, $Oh = \mu_0/\sqrt{\rho R\sigma}$, is small.

Zhang and Basaran [5, 56, 55] have studied fluid breakup, with emphasis on drop formation. They have utilized electric fields and piezo-electric nozzles to make drops on demand (DOD). Careful control of the waveforms that are input to the piezo nozzles have successfully eliminated satellite drops and even reduce the drop radius significantly below the nozzle radius [12]. Shore and Harrison [39] did studies of drops made from adding polyethylene oxide (PEO) to a low viscosity Newtonian solvent. They showed that satellite drops were suppressed by the elasticity as the liquid bridge is pulled either into the nozzle or the primary drop.

Figure 3–10 shows the position profile of the endplates and the master curve of a STB experiment, again performed with PS025. An exponential profile is imposed on the endplates, or ε_L, with very low rates. As seen in the master curve, the diameter seems to approach necking, *i.e.,* a vertical line, but strain-hardening causes the break-up to slow down. We also see that the lower the strain rate, the faster the break-up, as gravitational forces have increasing influence as the rate is decreased.

3.5 Filament Stretching Extensional Experiments

We now introduce the last type of extensional rheology experiment. These experiments, called filament stretching experiments, are more difficult to perform than capillary break-up and stretch-to-break experiments. The hardware has be to capable of reaching higher strains and strain rates, *i.e.,* larger range of motion and velocities. Along with advanced hardware comes advanced motion control. A capillary break-up experiment can be performed with a solenoid, which just requires a on/off switch. A stretch-to-break experiment with constant velocity can be achieved

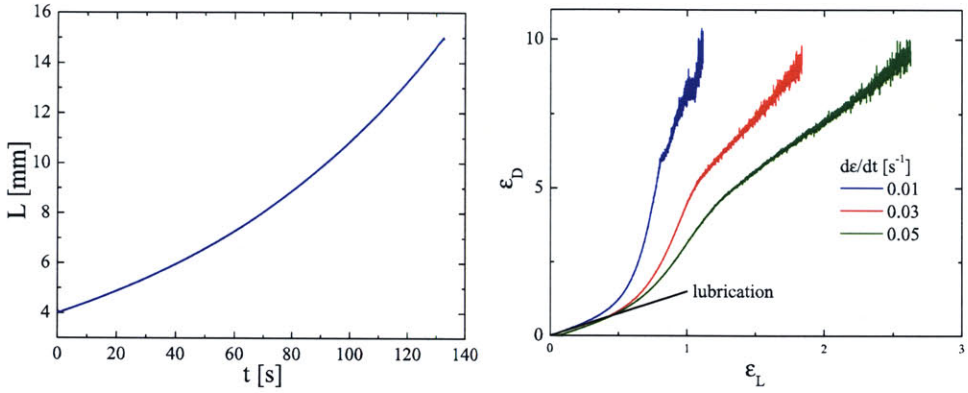

(a) position profile (b) master curve

Figure 3–10: Stretch-to-break experiments, performed with PS025.

with a DC rotary motor (utilizing a rack and pinion setup). A filament stretching experiment requires a linear motor that can be carefully controlled, and hence introducing complexity in both hardware and software. For a review of filament stretching rheometry of complex fluids, see [26].

A schematic of the filament stretching extensional rheometer (FiSER) is shown in figure 3–1. Two DC brushless linear motors traverse on a 2 m stage. The top motor is the top endplate that stretches the fluid. The bottom motor always moves at half the position and velocity of the top motor, marking the midplane of the fluid. The laser micrometer is mounted to the bottom motor, hence always measuring the midplane diameter of the fluid sample. The bottom endplate stay fixed, and is attached to the force transducer.

Figure 3–11 shows the position profile of the endplates and the master curve of a filament stretching experiment. As compared to figure 3–10, the radius does not experience necking early on as it does in STB experiments. Strain-hardening causes the filament to follow uniform elongational flow (UEF). As was the case in STB, lower rates corresponds to faster break-up. Furthermore, the strain rate also affects the fluid stress. Fluid stretched at higher rates experience increased contribution from the polymer stresses. We saw this from the discussion on the Deborah number, De,

in section 2.4.2), and we will see further evidence later in the results.

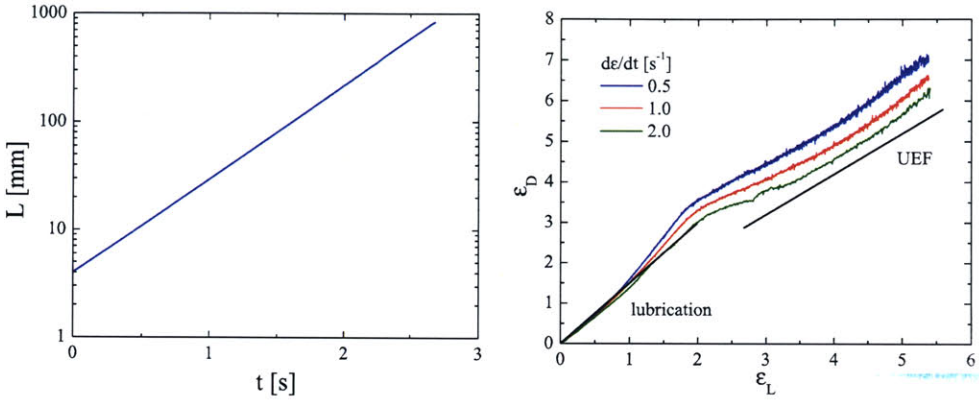

(a) position profile (b) master curve

Figure 3–11: Filament stretching experiments, performed with PS025.

Within a filament stretching experiment, we can further differentiate between three types:

Type I: In a type I experiment, the axial strain rate is fixed at a constant rate, $\dot{\varepsilon}_0 = \dot{\varepsilon}_L$. The diameter is assumed to decay at the uniform elongational flow (UEF) limit:

$$R_{UEF} = R_0 e^{-\frac{1}{2}\dot{\varepsilon}_0 t} \tag{3.3}$$

The Trouton ratio is then calculated as:

$$Tr_I = \frac{F_p(t)}{\pi R_{UEF}^2(t)\,\dot{\varepsilon}_0} \tag{3.4}$$

Type II: In a type two experiment, the axial strain rate is still constant, but the diameter is measured, instead of assumed. The Trouton ratio stays the same, except the diameter and the strain rate is now a measured quantity.

$$Tr_{II} = \frac{F_p(t)}{\pi R_{meas}^2(t)\,\dot{\varepsilon}_D(t)} \tag{3.5}$$

Type III: In a type III experiment, the radial strain rate (*i.e.*, the true strain

rate) is fixed. This means that the axial strains have to be manipulated in such a way that the diameter decreases at a steady exponential fashion. The Trouton ratio now becomes:

$$Tr_{III} = \frac{F_p(t)}{\pi R^2(t)\,\dot{\varepsilon}_0} \tag{3.6}$$

where $R = R_0 e^{-\frac{1}{2}\varepsilon_0 t}$, and ε_0 stays a constant through the duration of the experiment.

Figure 3–12 shows a schematic of the three types of filament stretching. The arrows indicate the flow of information. In type I, the only information being transmitted is the PMAC (controllers) to the motors. In type II, additional information is being transmitted from the laser micrometers to the DAQ (data acquisition) system. In type III, information is passed along from the DAQ system to the PMAC, hence closing the loop.

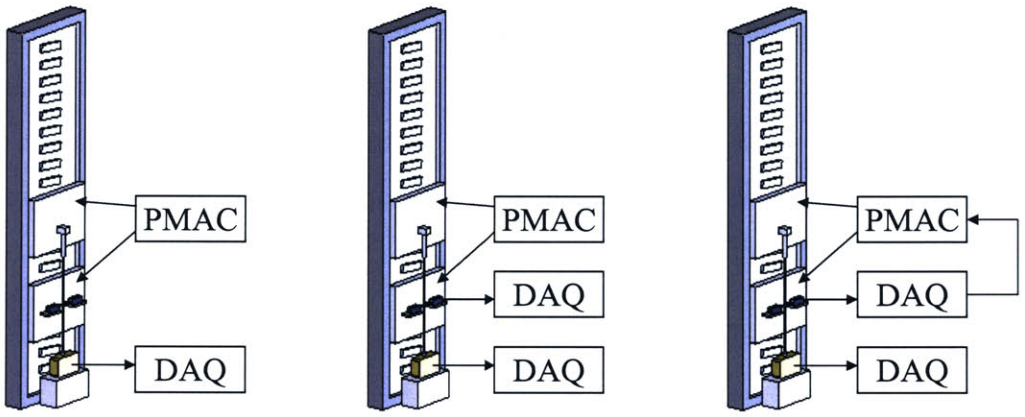

(a) Type I (b) Type II (c) Type III

Figure 3–12: Schematic of the three different types of filament stretching experiments. The PMAC (multi-axis controller) controls the two motors. Force and diameter readings (either one or both) are acquired through the data acquisition (DAQ) system. Even though the two readings are effectively collected by the same DAQ system, diameter and force acquisition are represented by two separate boxes to clarify the feedback path to the controller.

The key in these filament stretching experiments is remembering that we can only impose axial strains. In types I and II, the axial strain rate is fixed, so the

motion control can be simplified by either pre-determining the trajectory. In our implementation, we actually calculate the trajectory live in a type II experiment. However, because the input is a counter (the time step is fixed), these live calculations can be done quickly without causing any delay in the motion control. In a type III experiment, the axial strain rate is controlled so to result in a constant radial strain rate. We can not control the radial strain directly, so to hold the radial strain rate constant requires careful control of the axial strain. Calculations now depend on live measurements of the radius. The process of "converting" the radial strain measurement into an imposed axial strain adds further complexity to the calculation of the motor trajectories.

Other types of extensional rheology experiments can be performed. One of the most simplest is the constant force extension test. A weight is used a bottom endplate and let go, stretching the fluid as it falls under gravity [21]. Other methods include the Sentmanat Extension Rheometer (SER) Universal Testing Platform. The rheometer can be attached to a conventional shear rheometer. It consists of two rolling drums. The sample is clamped onto the two drums and stretched as the drums rotating in opposite directions. This rheometer is good for materials that are more elastic, ideal for melt rheology, tensile testing of solids, as well as testing for peeling, cut growth, and dynamic friction [38].

Chapter 4

Control Schemes for Filament Stretching Experiments

4.1 Previous Work

There have been previous efforts to perform a type III stretching experiment, in which the radial strain rate remains constant during the course of the experiment. Remember from the previous chapter that type III experiments are the most complex in that they require sophisticated hardware *and* software. Constant force experiments, the most primitive type of filament stretching experiments, were done by Matta and Tytus with a falling weight as the bottom endplate [21]. Sridhar *et al.* then built an extensional rheometer with linear motors, allowing the capability of performing type II experiments [43,48]. Type III experiments were not achieved until years later, when Orr and Sridhar used an iterative method [29]. The strain rates were calculated after each experiment, and the axial profile adjusted to compensate for rates too fast or slow. This worked, but was a tedious process, and can easily be affected by initial conditions. Two stretching experiments with the same axial profile does not always result in the same radial strains and strain rates.

Anna tried a PID controller (proportional-integral-derivative) with the system [2]. A commanded diameter, D_{cmd}, was first determined for each time step by the following computation:

$$D_{\text{command}}(i+1) = D_{\text{ideal}}(i+1) + K_P \delta D(i) + \frac{K_D}{\Delta t}[\delta D(i) - \delta D(i-1)] + K_I \Delta t \sum_{j=0}^{i} \delta D(j) \tag{4.1}$$

Here, $\delta D(i) = D_{\text{ideal}}(i) - D_{\text{command}}(i)$ is the error in diameter, and K_P, K_I, and K_D are the proportional, integral, and derivative gains in the PID controller. Once a commanded diameter is determined, it must be converted into a length, or motor position. The conversion from radial to axial strain is stated in general form as:

$$L_p(i+1) = L_p(i) \left[\frac{D_{\text{measured}}(i)}{D_{\text{measured}}(i+1)} \right]^{p(i)} \tag{4.2}$$

where $p = 2$ for the uniform elongational flow limit and $p = 4/3$ for reverse squeeze flow, as covered in section 2.2.1.

This active control PID method resulted in large noises in the force measurement, predominantly coming from the vibrations of the motor as it tries to maintain a steady strain rate. Figure 4–1 shows that the force measurements obtained from a PID controlled experiment results in force readings that are masked by erratic noise.

Anna then tried an open loop method in which the "slope" of the master curve is used to determine the endplate position necessary for a constant radial strain rate. A type II experiment was first run, with the axial strain rate $\dot{E} = \dot{L}/L$. The axial velocity is defined as $V_z = \dot{L}S$, where S is a dimensionless velocity. The mid-plane diameter can then be related to the endplate separation as:

$$\frac{dD_{mid}}{dt} = -\frac{1}{2} D_{mid} \left(\frac{\dot{L}}{L} \right) S' \tag{4.3}$$

where, S' is the derivative of S with respect to a dimensionless length, $\zeta = z/L$. Combining the definitions and equation 4.3, we get an effective strain rate, or true strain rate, of:

$$\frac{\dot{\varepsilon}_{\text{eff}}}{\dot{E}} = S' \tag{4.4}$$

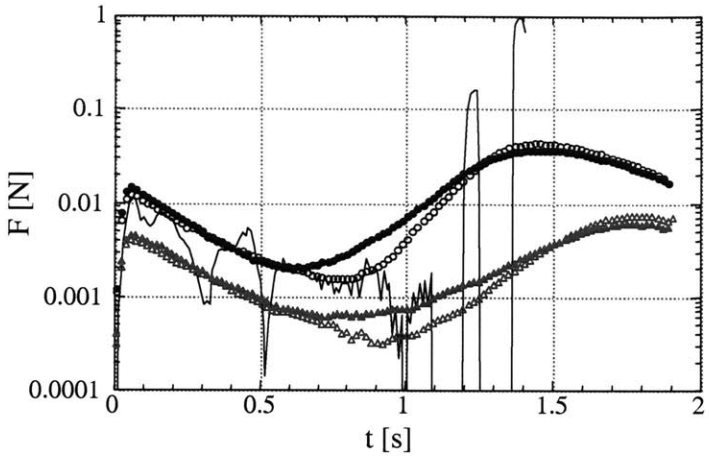

Figure 4–1: Force measurements from type II and type III experiments. The filled symbols represent type II data. The hollow symbols represent data from a type III experiment utilizing an open-loop technique. The black line shows the results from type III experiment utilizing PID control. The different shapes represent two different fluids tested - PS05 (○) and BG1 (△). See [2] for details.

Replacing the strain rates with diameter and length:

$$\frac{\frac{d}{dt}\ln\left(D/D_0\right)}{\frac{d}{dt}\ln\left(L/L_0\right)} = -\frac{1}{2}S' \tag{4.5}$$

Eliminating the dt yields

$$\frac{d\ln\left(L/L_0\right)}{d\ln\left(D_0/D\right)} = \frac{2}{S'} \tag{4.6}$$

This shows that S' is effectively a measure of the slope of the master curve. It can be used to achieve a type III experiment by imposing a endplate separation of:

$$L = L_0 e^{\int \left(1/S'\left(\varepsilon_{D,\text{ideal}}\right)\right) d\varepsilon_{D,\text{ideal}}} \tag{4.7}$$

Here, S' is re-defined as a function of strain, ε_D by re-writing S' as $S'\left(t\right) = S'\left(t\left(D_{mid}\right)\right) = S'\left(\ln\left(\frac{D_0}{D}\right)\right)$. Hence, if $\varepsilon_{D,\text{ideal}}$ is defined to grow at a constant rate, $\varepsilon_{D,\text{ideal}} = \dot{\varepsilon}_0 t$, then equation 4.7 will result in a type III experiment.

Spiegelberg et al. was able to achieve type III stretching experiments with a trial

and error method [41]. The diameter was modelled to decay as a superposition of two exponential functions:

$$V_p(t) = L_0 k_1 e^{k_1 t} e^{-\alpha t} + k_2 \left(L_0 e^{k_2 t} - d_0\right)\left(1 - e^{-\alpha t}\right) \tag{4.8}$$

d_0 is a measure of the critical strain (when filament starts to strain-harden), k_1 and k_2 are parameters to be fine-tuned for each fluid and strain rate.

These methods all worked but relied on prior measurements. The trial and error method required many runs to get a good estimate of the two unknown parameters. Anna's open loop method relied on the master curve slope from previous measurements. And even though the master curve is well behaved and can be predicted for a large range of strain rates, no two experiment will produce exactly the same curves temporally. That is, if we were to plot the two strains with time, there would be offsets which would depend on initial conditions and fluid sample "defects" that can not be controlled. All this motivates a control scheme that is more robust and more flexible. It would be ideal to produce a method that could achieve type III steady flow with one run, and can adjust to the different initial conditions of each run. This would mean that the method could measure the changing parameters, or S' in Anna's method, as the stretching experiment runs.

4.1.1 Adaptive Control

A previous method we tried involved adaptive control [40], in which an parameter can adapt to the system throughout the experiment. For example, take the following 2nd order system:

$$m\ddot{x} + b\dot{x} + kx = F(t) \tag{4.9}$$

Here, m, b, and k refer to the mass, damper, and spring, respectively. F is the force that is input, and x is the position of the mass. If all the parameters - m, b, and k - are known, then for any desired position, $x_{desired}$, we can always pick an input that will result in the desired position. Complexity arises when the parameters are

unknown or varying with time. For example, a robotic arm that is made to catch a projectile does not know the mass of the projectile. Or a ship trying to control its trajectory may meet varying wind velocities. This is where adaptive control becomes useful.

We can consider Anna's PID scheme, in which a conversion from radial to axial strain was required. This conversion relied on the time-varying parameter $p(i)$. A controller built to account for the varying p would be able to provide a profile resulting in a type III experiment. We represent the filament stretching experiment into a 0th order system:

$$\frac{L_p}{L_0} = \left(\frac{R_0}{R}\right)^p \tag{4.10}$$

We assume that the length and radius are related by the exponent p that varies in time. We want to control R by controlling L_p. We rewrite this as:

$$a \ln(x) = \ln(\text{input}) \rightarrow ay = u \tag{4.11}$$

We pick a reference model $a_m y_m = r$ and use the controller $u = \hat{a}_r r$. The error is defined error as $e = y - y_m$. We can use the adaptation law:

$$\dot{\hat{a}}_r = -\gamma e r \tag{4.12}$$

where γ cab be thought of as an adaptive gain. If we choose $a_m = 1$, then we get a desired trajectory:

$$y_m = r = \ln\left(\frac{R_0}{R_d}\right) = \ln\left(\frac{R_0}{R_0 \exp(-0.5\dot{\varepsilon}\, t)}\right) = 0.5\dot{\varepsilon}\, t \tag{4.13}$$

One thing to note is that if a is known, then we can choose the controller to be $u = a_r^* r$, with $a_r^* = a/a_m$. This would result in $e = 0$, *i.e.*, an output that follows the desired value perfectly.

Figure 4–2 shows the schematic of the adaptive control scheme.

We were able to simulate adaptive control by making up a polynomial for p,

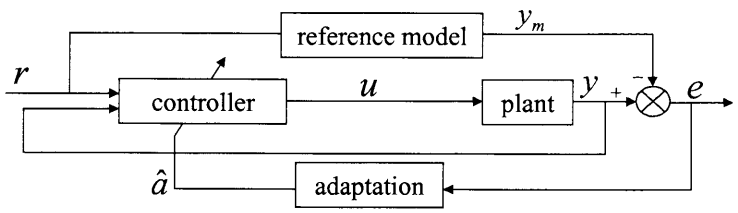

Figure 4–2: Schematic of the adaptive controller.

effectively making up the dynamics of the fluid. Using this response for the fluid, simulations showed that the top endplate was able to stretch the fluid so that the mid-plane radius decayed at a constant rate. In implementation, the system became very complicated. Difficulty arose in following the behavior of the controller. Furthermore, the cost of calculation was high because of the complexity, introducing delays.

4.2 Euler Method

To keep things simple, we decided to use a more primitive method. For every iteration in time, the changes in radial and axial strains are determined. Assuming that the two strains will behave similarly, e.g. increase and decrease in the same manner, for the next time step, we calculate the necessary axial strain to impose in order to obtain a desired radial strain. Remember that in our system, the axial strain is controllable and the radial strain is measurable.

The Euler first order approximation method is essentially fitting a line between two points. The slope of the line is the value that is important. Axial and radial strains are parameterized by time, so we need to calculate the slope with time. At each iteration, i, the present strains are measured. A "slope" is then computed with the strains from the previous iteration, $i-1$. This slope is essentially the same S' value that Anna used in her open loop control. The slope can be thought as $\Delta\varepsilon_L/\Delta\varepsilon_D$ and is thus defined as:

$$\frac{\Delta\varepsilon_L}{\Delta\varepsilon_D} = \frac{\varepsilon_{L,\text{cmd}}(i) - \varepsilon_{L,\text{cmd}}(i-1)}{\varepsilon_{D,\text{meas}}(i) - \varepsilon_{D,\text{meas}}(i-1)} \tag{4.14}$$

Figure 4–3 shows a schematic of the Euler method. With this slope calculation, we can command the axial strain with:

$$\varepsilon_{L,cmd}(i+1) = \varepsilon_{L,cmd}(i) + \left[\frac{\varepsilon_{L,cmd}(i) - \varepsilon_{L,cmd}(i-1)}{\varepsilon_{D,meas}(i) - \varepsilon_{D,meas}(i-1)}\right] \left[\varepsilon_{D,ideal}(i+1) - \varepsilon_{D,meas}(i)\right] \tag{4.15}$$

The ideal radial strain is $\varepsilon_{D,ideal} = \dot{\varepsilon}_0 t$, with the radial strain rate constant, $\dot{\varepsilon}_D = \dot{\varepsilon}_0$.

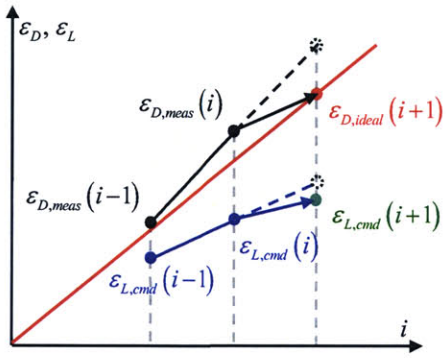

Figure 4–3: Schematic of the Euler method.

The main issue with the Euler method is the sensitivity of the slope calculation. As the radius grows smaller and smaller, the effects of noise increases. This can result in a slope that negative, or infinity. We explain this in further detail in the following section. Another source of problem is the difference between current and ideal radial strain. It is very possible that the current strain might have exceeded the desired strain for the next iteration, making the slope term negative. This results in an axial strain that is lower for the next iteration, i.e. moving the motors down. Oscillations in the motors is by far the largest source of mechanical noise, which is transmitted to the force transducer. We see the effects of this in section 5.3.

4.2.1 Noise Problems

Figure 4–4 shows radius measurements taken from a stretching experiment. The red box represents a span of 0.1 s. The first inset shows that initially, measurements taken over the time step, 0.1 s, show a clear change in radius. The second inset shows the problem that results from noise when the change in radius over a time step is on the order of 25 μm. The radius measurements is enveloped by a band of ± 10 μm noise. The height of the red box becomes more and more flat, i.e. the change radius approaches zero, and even negative. This means that the slope, $\Delta\varepsilon_L/\Delta\varepsilon_D$, can approach $\pm\infty$. With slope being the defining parameter in our control scheme, this problem causes the control scheme to break down.

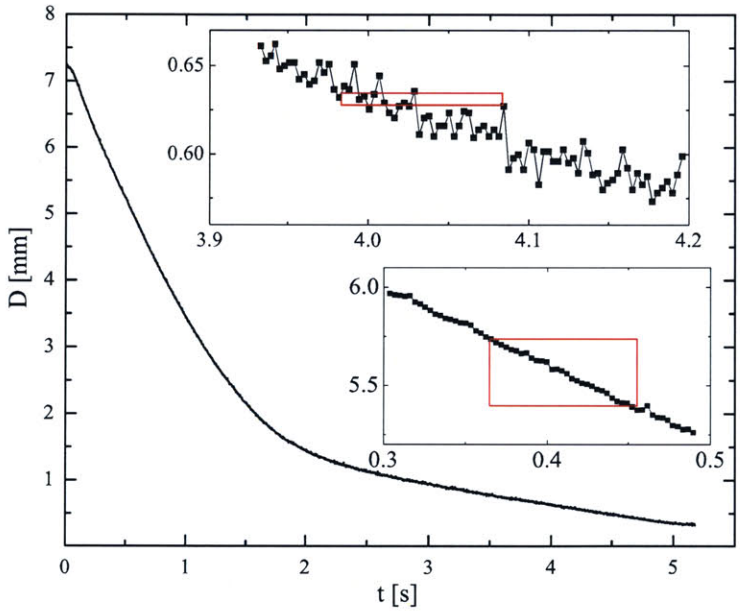

Figure 4–4: Effect of noise on radial strain measurements. The width of the red boxes represent a 0.1s time step.

The easiest way to go around this problem is to pick a larger time step so that the change in radius will be large enough and less likely to be affected by the noise. The trade-off with this fix is that the control is now refreshing more slowly, which means changes within the time step will not be captured within an iteration. This becomes

a larger problem when strain rates are large.

We tried two other ways to reduce the noise problem. We noted that the lower limit to which we could push the time step was 80 ms. Any lower and the effect of noise would cause oscillations in the motors. Instead of taking one radius measurement at every iteration, we take five measurements very fast and take the average. The PMAC takes about two to three cycles - each cycle being 442 μs - to collect five points.

Another method is to calculate with every other pairs of strain measurements. This was shown to work in numerical simulation by Peter Szabo, who was also able to simulate the noise problems. In this fashion, the control loop can still be iterated at the same time step, but the effective time step which is being used for the slope calculations is two time steps. Szabo was able to fix the noise problem with this method in numerical simulations. We see, however, in figure 4–5 that this method does not fix the noise problem. In fact, none of the methods listed above were able to prevent the slope $\Delta\varepsilon_L/\Delta\varepsilon_D$ from oscillating erratically.

4.3 Least Square Approximation

In order to get a longer effective time step but not losing information, we tried a least squares approximation method. In this scheme, the slope of the strains is calculated with four pairs - each pair being radial and axial strains - of points, as opposed to two pairs in the Euler scheme. We were able to update our iterations twice as fast, 40 ms, while calculating the slope with a linear least squares regression:

$$\frac{d\varepsilon_L}{d\varepsilon_D} = \frac{n\left(\sum_i \varepsilon_{L,i}\varepsilon_{D,i}\right) - \left(\sum_i \varepsilon_{D,i}\right)\left(\sum_i \varepsilon_{L,i}\right)}{n\left(\sum_i \varepsilon_{D,i}^2\right) - \left(\sum_i \varepsilon_{D,i}\right)^2} \tag{4.16}$$

The commanded axial strain is still determined in the same way as before, *i.e.*, as according to equation 4.15.

Least squares approximation proved to be a good way to smooth out the errors caused by noises in radius measurements. If we compare the ratio of changes in

strains, the driving factor in the control algorithm, we can see the improvements this has over the Euler method, and the Euler variations.

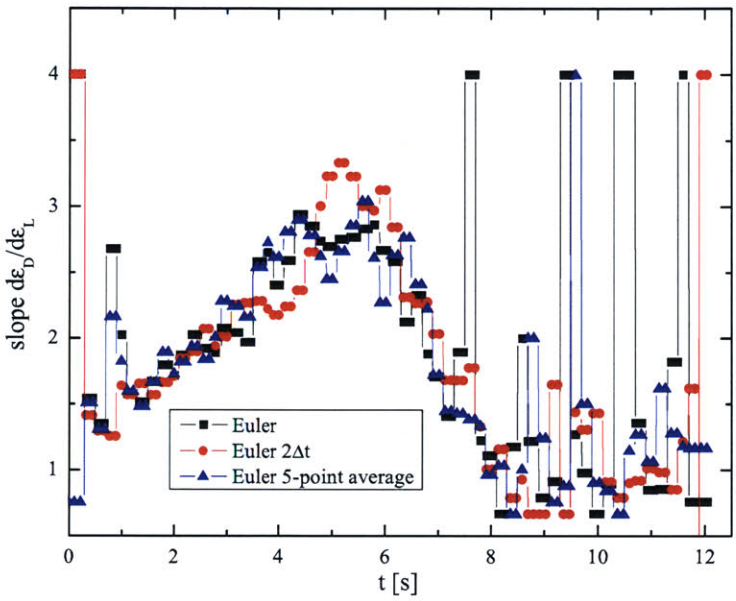

Figure 4–5: Comparison of the slope with different control algorithms.

Figure 4–5 shows the comparison of the various algorithms. The Euler method and its variations show no real improvements in any aspect. The ratio of slopes become "unstable" at relatively the same strain. We define $\Delta\varepsilon_L/\Delta\varepsilon_D$ to be unstable when it hits the upper or lower maximum, which is set generously above and below the maximum and minimum values that we expect. Figure 4–6 show the same comparison for motor position and diameter measurements. The motor position results show that the profile is comparable in each case, with smooth trajectories up to $t = 8$ s, then showing similar oscillations.

4.4 Other Considerations

Other variations of the least square approximation is a weighted calculation. With the linear least squares regression, a line is fit through the four points, with each

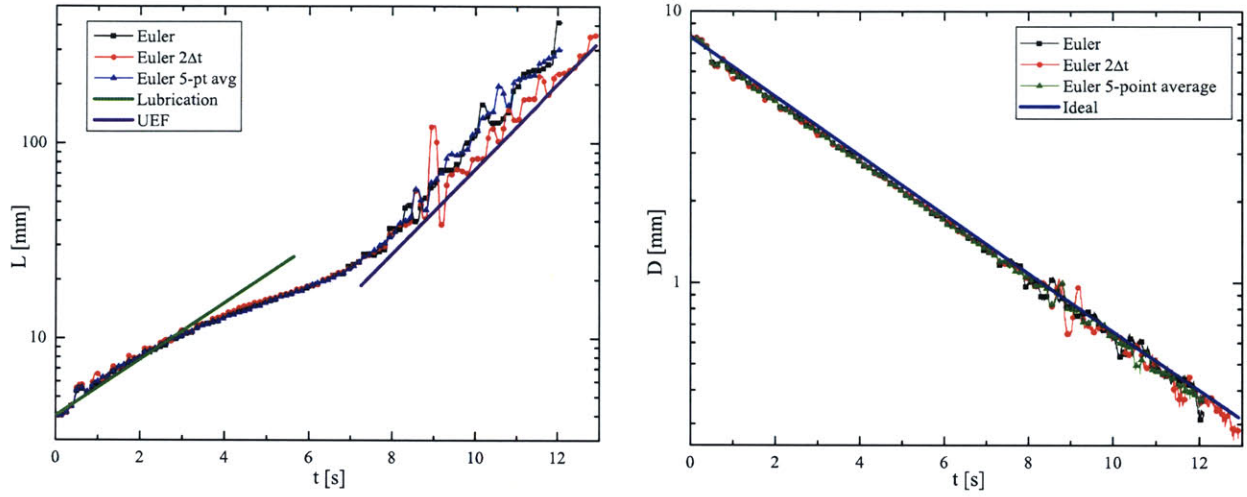

Figure 4–6: Position and diameter comparisons of the Euler method with its variations.

point given equal significance. A "smarter" way to do this would be to weight the latest points more than the older points, as they would be a better representation of the master curve at the present moment. This can be implemented by using a Taylor expansion series of the strains at various iterations:

$$y_{i+1} = y_i + \delta x y' + \frac{1}{2}\delta x^2 y'' + \frac{1}{6}\delta x^3 y''' + \cdots \tag{4.17a}$$

$$y_{i-1} = y_i + (-\delta x)\, y' + \frac{1}{2}(-\delta x)^2\, y'' + \frac{1}{6}(-\delta x)^3\, y''' + \cdots \tag{4.17b}$$

$$y_{i-2} = y_i + (-2\delta x)\, y' + \frac{1}{2}(-2\delta x)^2\, y'' + \frac{1}{6}(-2\delta x)^3\, y''' + \cdots \tag{4.17c}$$

$$y_{i-3} = y_i + (-3\delta x)\, y' + \frac{1}{2}(-3\delta x)^2\, y'' + \frac{1}{6}(-3\delta x)^3\, y''' + \cdots \tag{4.17d}$$

Here, y', y'', y''', and y^4 refer to the first, second, third, and fourth derivatives, respectively, of y with respect to x. To apply this two our system, we take y to be $\Delta\varepsilon_L$ and x to be $\Delta\varepsilon_D$, so that $y' = \frac{\Delta\varepsilon_L}{\Delta\varepsilon_D}$. The goal is to obtain a good estimate of y'. To do this, we take linear combinations of 4.17. The number of equations used will

determine the error. The more points, *i.e.,* equations, the more higher order terms (y'', y''', ...) we can eliminate, and hence the smaller error. With two prior points, the prediction for y' is:

$$\frac{3y_i - 4y_{i-1} + y_{i-2}}{2\delta x} = y' - \frac{1}{3}\delta x^2 y''' + O\left(y^4\right), \tag{4.18}$$

where the error, $-\frac{1}{3}\delta t^2 y''' + O\left(y^4\right)$, to first order approximation, scales with δx^2. Using more points, the error can be pushed to scale with higher orders or differentiation. Equation 4.18 shows the same approximation of y' with one extra point:

$$\frac{11y_i - 18y_{i-1} + 9y_{i-2} - 2y_{i-3}}{6\delta x} = y' - \frac{1}{4}\delta x^3 y^4 + O\left(y^5\right) \tag{4.19}$$

The difficulty with implementing this scheme with the system is that the independent variable, ε_L, does not change in equal increments with each iteration, as δt is different for each step. This means the calculations become more computationally more expensive. Furthermore, quick simulations show that the Taylor expansion method can lead to irregularities, over- and under-predicting strains. This would cause aforementioned motor oscillations.

4.5 Other Closed-Loop Methods

Bach *et al.* has recently achieved a closed-loop control of their FiSER, which is also capable of performing constant true strain rate stretching experiments [3]. They had previously used the iterative Orr-Sridhar method [4]. The paper deso not give details on the control algorithm, and is only briefly mentioned as a closed loop proportional regulator scheme in [34]. In this new closed-loop method, the top motor, *i.e.,* top endplate, will actually move closer to the bottom endplate when the filament starts to break-up. During break-up, the filament necks so fast that the diameter is decaying faster than an exponential rate even if the top endplate is held constant. The only way to "slow" down the necking is to move the plates closer together again.

The fluid used in these studies [34, 3] were polyethylene and polystyrene melts,

and the strain rates are very low, ranging from $\dot{\varepsilon}_D = 0.003 - 0.3\ \mathrm{s}^{-1}$. For reference, the strain rates we perform are much higher, and order of magnitude higher than their fastest rate. Low strain rates are easier to control because it allows the time step to be larger. Bach's method of bringing the top plate closer when necking occurs too rapidly allows the experiments to reach higher strains than the previous iterative methods, reaching $\dot{\varepsilon}_D \sim 7$. In our control algorithm, we include a safety feature that does not allow the top endplate to ever move closer to the bottom endplate. The motion program is stopped if the next motor position is smaller than the current position.

Chapter 5

Rheology of a Dilute Polymer Solution

We have presented the set of hardware that gives us the ability to to stretch a fluid in chapter 3 and also an algorithm to control the hardware in 4. We now move into the heart of the project - measuring material properties and studying the rheology of the polymer solution of interest.

5.1 Fluid - PS025

The fluid that we used extensively in our studies is a polymer solution. It consists of polystyrene dissolved in styrene oil, with a concentration of 0.025% by weight, hence the name PS025. This concentration is far below the critical coil overlap concentration, $c*$, of 0.091%. The ratio $c/c* = 0.274$ means that this solution is a dilute solution. For a more detailed discussion on concentration in regards to dilute-ness, see [18].

PS025 is a Boger fluid, [1] which is a model visco-elastic fluid. Theoretical and experimental rheologists in the 1970's searched for a fluid with elastic properties while exhibiting an apparent viscosity that is constant for a large range of shear

[1] Named after David Boger, and first called "Boger fluid" by Walters [50].

rates. Such a fluid would allow them to study "fluid elasticity" by comparing the fluid response with that of a Newtonian liquid. Boger made such a fluid by dissolving a high molecular weight polymer in a high viscosity solvent [8,10,9]. This combination results in high elasticity and non-shear-thinning properties, as explained by the elastic dumbbell theory for dilute solutions [32,7]. The PS025 used in our experiments was prepared by Anna [2].

Table 5.1 shows some of the important properties of the PS025 solution that was used in all of the filament stretching experiments.

Table 5.1: *Fluid properties of PS025.*

Fluid	PS025
λ [s]	5.02
Solvent visc. η_s [Pa.s]	45.5
Total visc. η_0 [Pa.s]	49
Surf. tension σ [mN/m]	38
Density ρ [kg/m^3]	1026
Extensibility $L^2[\sim]$	4606

5.2 Shear Rheology

Before we start analyzing the extensional rheology of PS025, it is necessary to discuss its shear rheology. Shear rheology data were taken with the AR1000 (TA instruments) with a 4 cm diameter conical plate. See figure 5–1 for a schematic of the rheometer. The conical plate, with a 2° angle, induces a flow such that the fluid sample experiences the same shear rate throughout its entire volume. The shear viscosity can be calculated by:

$$\eta = \frac{3T}{2\pi R^3 \dot{\gamma}} \tag{5.1}$$

where T is the torque required to spin the cone at a frequency ω, and $\dot{\gamma}$ is the shear rate given by $\dot{\gamma} = \omega/\theta$.

The shear viscosity of PS025 is very sensitive to temperature. It increases exponentially with temperature drop. For this reason, we need to have a good estimate of

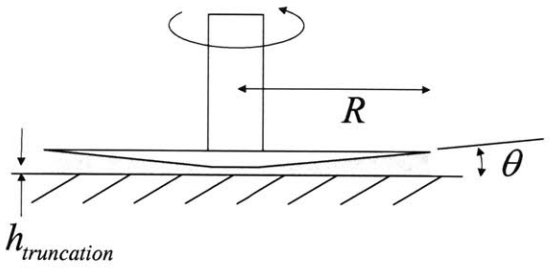

Figure 5–1: Schematic of the cone and plate rheometer and the relevant geometries.

the viscosity at all temperatures as it directly affects extensional viscosity measurements. The temperature at which the filament stretching rheometer operates can not be controlled, as it is set by the ambient temperature. The operating temperature can vary anywhere from $20 - 24°C$. To capture the change of viscosity with temperature, we use time-temperature superposition. We define a function, a_T:

$$a_T(T_0) = \frac{\eta(T)}{\eta(T_0)} \tag{5.2}$$

where T_0 is a reference temperature that is arbitrarily chosen. This function is empirically fitted by the Williams-Landel-Ferry (WLF) equation:

$$\ln(a_T) = \frac{-c_1^0(T - T_0)}{c_2^0 + (T - T_0)} \tag{5.3}$$

Figure 5–2 shows how $\ln(a_T)$ changes with temperature. In a shear rheometer, the temperature can be easily regulated by the Peltier plate and water cooling system (Julabo F25). In the FiSER, the operating temperature is governed by the ambient temperature. There have been attempts to incorporate an oven around the length of the FiSER, but it is difficult to maintain constant temperature everywhere. A temperature gradient along the length of the FiSER would induce airflow, adding effects to the fluid flow that we would not be able to measure. Therefore, all experiments were done in open air, where temperature can vary from day to day, even hour to hour. This can become a nightmare for rheological measurements because, as shown in figure 5–2, viscosity is highly sensitive to temperature. Figure 5–2 shows the vis-

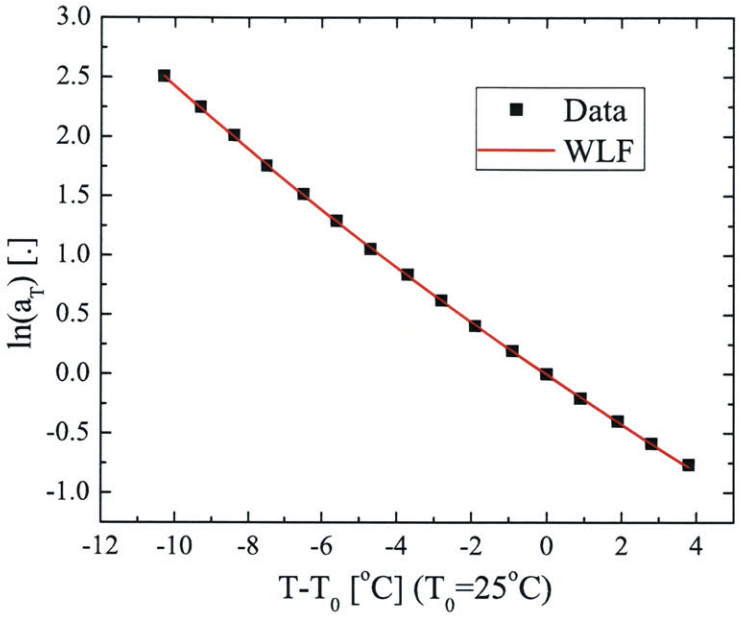

Figure 5–2: Viscosity dependence on temperature, as represented by the function $a_T = \eta(T)/\eta(T_0)$. The experimental data are fit to the Williams-Landel-Ferry (WLF) model, with $c_1^0 = 19.5$ and $c_2^0 = 90.3$. The reference temperature is $T_0 = 25.3°\text{C}$.

cosity at a stress of 100 Pa · s for temperatures ranging from $15 - 30°C$. The viscosity spans more than an order of magnitude, from $20 - 500$ Pa · s.

We can determine the zero-shear-rate viscosity, η_0, as well as the solvent viscosity, η_s, by looking at the dynamic viscosity, η', across a range of shear rates. We expect the zero-shear rate viscosity to be the limit as shear rate approaches zero, and the solvent viscosity to be the limit as shear rate approaches infinity.

$$\lim_{\dot{\gamma}\to 0} \eta' = \eta_0 \tag{5.4a}$$

$$\lim_{\dot{\gamma}\to \infty} \eta' = \eta_s \tag{5.4b}$$

Figure 5–3 shows the dynamic viscosity measurements for a range of shear rates at $T = 15°\text{C}$. The difference between the zero-shear rate viscosity and the solvent viscosity is the viscosity contribution from the polymer, η_p.

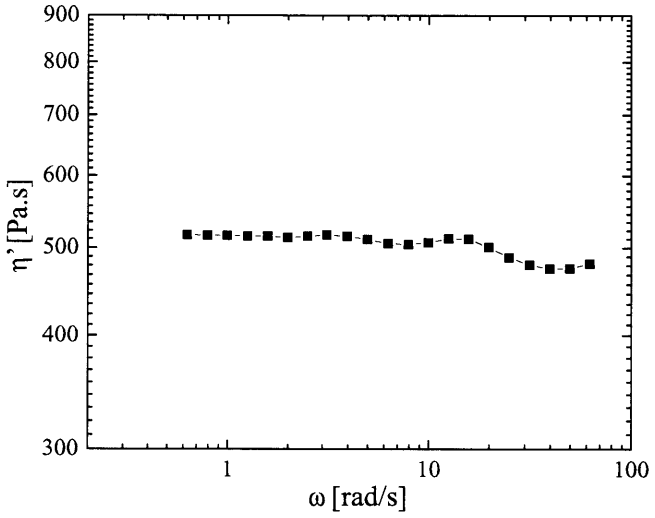

Figure 5–3: Dynamic viscosity of PS025 at $T = 15°C$.

5.2.1 Oscillatory Shear Flow

To measure the storage and loss modulus, G' and G'', respectively, we run oscillatory shear tests on the rheometer. We impose a flow of the form

$$\gamma = \gamma_0 \sin(\omega t) \tag{5.5}$$

This gives us a shear rate of:

$$\dot{\gamma} = \gamma_0 \omega \sin(\omega t) \tag{5.6}$$

The stress that arises from this oscillatory shear is represented by:

$$\tau_{12} = G'(\omega)\,\gamma_0 \sin(\omega t) + G''(\omega)\,\gamma_0 \cos(\omega t) \tag{5.7}$$

G' and G'' are the storage and loss moduli introduced in section 2.3.4. We would like to determine the two moduli at a wide range of shear rates. To achieve this, we would nominally need to oscillate the rheometer at very high and very low angular frequencies. The AR1000 has a maximum motor speed of 100rpm, or 628 rad/s. It

can reach very low rates, but these values tend to be erratic as the force readings reach the resolution of the instrument. Time-temperature superposition helps us make rheological measurements that are outside the effective range of the rheometer. The shear rate and temperature can be related by a shift factor.

First we pick a reference temperature. To get rheological measurements above the maximum frequency of the rheometer, we decrease the temperature and run the experiments again. Rheological data below a certain shear rate at the reference temperature might be too close to the instrument resolution to measure. We can get around this by increasing the temperature and running the same experiments. The data from these experiments performed at different temperatures can be superposed into a master curve by introducing shift factors in the x- and y-axes. Figure 5–4 shows the storage and loss moduli of PS025 over an effective shear rate range of $0.06 - 10,000\text{rad/s}$, with reference temperature set at 20°C. Table 5.2 shows the shift factors that were generated by the TA software (Rheology Advantage Data Analysis, V5.0.38).

Table 5.2: *Time-temperature superposition shift factors for PS025.*

Temperature	x-shift	y-shift
10	1.204	0.01507
15	0.554	0.00747
20	0.0	0.0
25	-0.518	-0.00735
30	-0.976	-0.01457

5.3 Extensional Rheology

Extensional viscosity can be determined by measuring the fluid stresses, which can be calculated with equation 3.1, and then using the definition given by equation 2.12. In dimensionless form, it is represented by the Trouton ratio, Tr, as explained in section 2.2.2. We now show the results for type II and type III experiments.

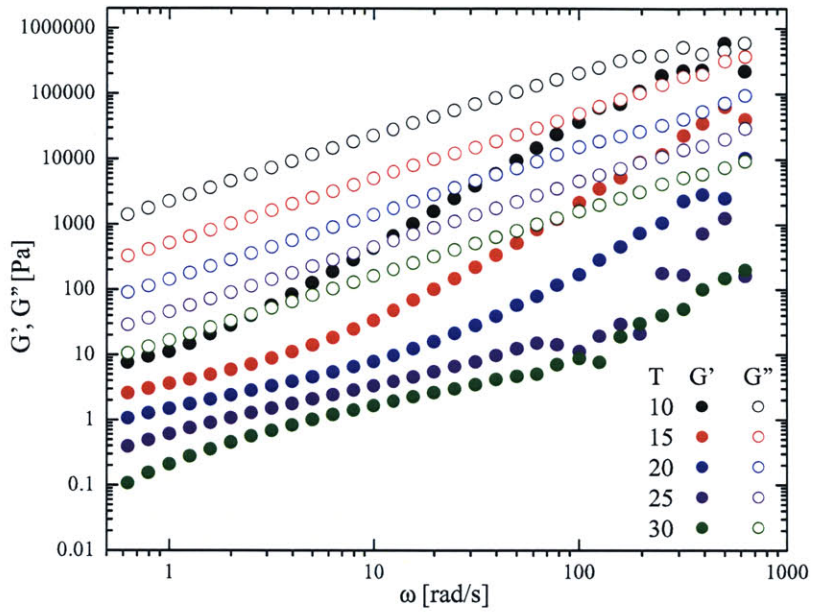

(a)

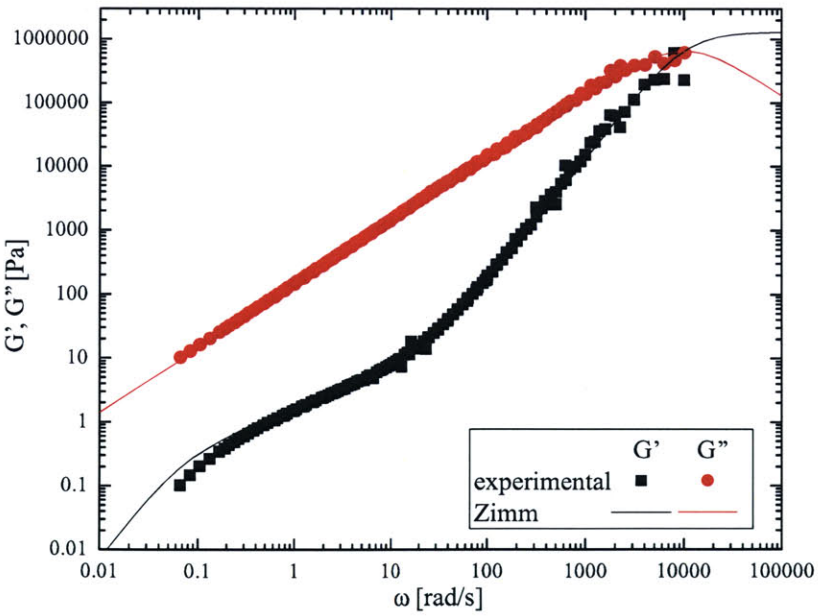

(b)

Figure 5–4: Experimental values for G' and G'' and the theoretical prediction given by Zimm theory. The reference temperture is set at 20°C. The Zimm relaxation time is $\lambda_Z = 13.58$ s.

5.3.1 Type II Results

The goal of the study is to understand how the extensional viscosity grows for a given strain rate. Before we present start presenting the results for the constant rate results, we first show the results from type II (constant nominal strain rate) experiments. These experiments are very simple to implement, as the motor trajectories are predetermined, or can be calculated without feedback from the other components of FiSER. We compare the data with the theoretical model, which assumes constant true strain rate, presented in section 2.4. The discrepancy will motivate the need for a type III approach.

Figure 5–5(a) shows the radial strain as a function of time from a type II experiments. A line of constant slope on this plot would imply a constant strain rate. The radial strain clearly experiences varying rates. In a type II experiment, the nominal strain rate is kept constant, so the the x-axis in figure 5–5(a) can be replaced with nominal strain rate using the substitution $\varepsilon_L = \dot{\varepsilon}_L t$. Doing this would give us the master curve, shown in figure 5–5(b). Note that the data agree with the lubrication and uniform elongational flow (UEF) limits.

Figure 5–6 shows the Trouton ratio, Tr, for type II experiments for a range of strain rates. The limit for initial times, $t \approx 0$, is $Tr \sim 1$ and not $Tr \sim 3\eta_s/\eta_0$ as expected from section 2.2.1. We will discuss this later in section 5.4. We see that type II experiments produce transient extensional viscosities that are higher than the FENE-PM predictions. This is because the radial strain rate is larger than the nominal strain rate. This causes the stresses from the polymer to be larger than the model.

To see why type II fails to match the FENE-PM model, which models the true strain rate as a constant value, we look at the strain rates in a type II experiment. See 5–7. In the top figure, 5–7(a), we see the absolute strain rate for various imposed rates. In the bottom figure, we normalize the strain rates by the axial strain rate, $\dot{\varepsilon}_L$, which is held constant. This ratio of the rates is effectively the slope of the master curve, $d\varepsilon_D/d\varepsilon_L$, as the dt terms can be canceled out. As mentioned previously, we

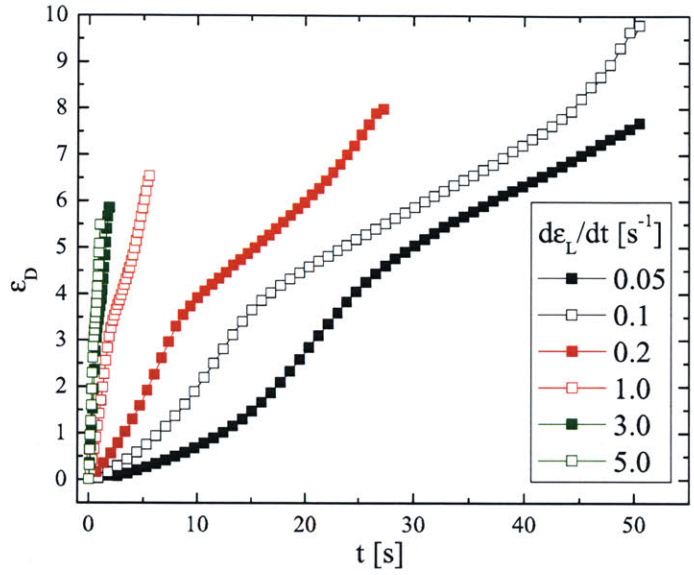

(a) Strain rate

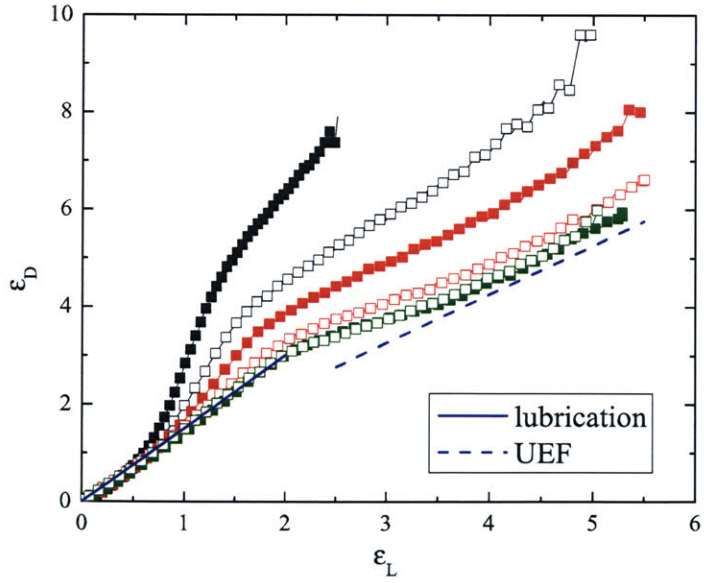

(b) Master Curve

Figure 5–5: Strain rates and master curves from type II experiments.

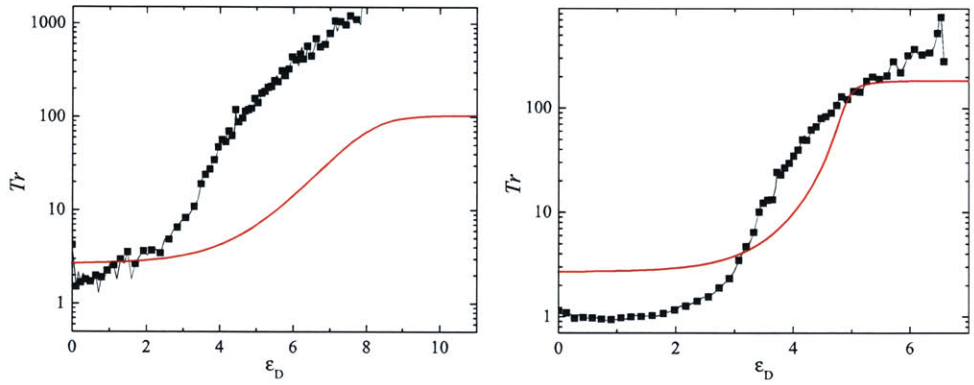

(a) 0.2 (b) 1.0

(c) 3.0 (d) 5.0

Figure 5–6: Trouton ratio, Tr, as a function of true strain, ε_D, for type II experiments. The red lines are the FENE-PM models for the respective strain rates.

see that the radial strain rate is higher than the nominal strain rate throughout most of the experiment, *i.e.,* the ratio of strain rates is greater than one, $\dot{\varepsilon}_D/\dot{\varepsilon}_L > 1$. This is why the polymer stresses grow faster than the FENE-PM model, which takes the radial strain rate to be constant, $\dot{\varepsilon}_D = \dot{\varepsilon}_0$.

5.3.2 Type III Results via Euler

Just as shear rheological data are determined at either fixed stress or strain rate, we want to have a constant parameter that can be adjusted when taking extensional rheological data. This is why so much work has been put into achieving a type III (see section 3.5) stretching experiments. Similar procedures can also be used to achieve a constant stress stretching experiment, but that would required force feedback as well as mid-plane diameter, adding another source of noise and complexity.

We now present results from type III experiments. These are experiments in which the motor trajectories are closely controlled, either from previous experimental data or with active control, such that that radial (true) strain rate is constant. Figure 5–8 shows the radius decay in terms of radial strain, from four Euler type III experiments. The blue lines indicate the ideal behavior. The experimental data deviates from the ideal lines. The experiments with the higher rates, $\dot{\varepsilon}_D = 1.91$ and $1.99\ \mathrm{s}^{-1}$, follow the ideal curves more closely, and hence, as we will see shortly, produce the best results. The deviations are caused by the instability of the Euler method, as discussed in section 4.2.1.

We present the data for the Trouton ratio, Tr, from an Euler type III experiment. See figure 5–9. The Trouton ratio follows the model as predicted by FENE-PM, but there is too much noise. This is expected as the radial strain often deviated from the ideal constant strain rate curve. Out of the four experiments shown in figure 5–9, only the last one, *i.e.,* $\dot{\varepsilon} = 1.99\ \mathrm{s}^{-1}$, produced results that can be compared with the model. It is not surprising this experiment was also the one with the smoothest strain rate, as shown in figure 5–8. The instability is an apparent weakness of the Euler scheme. This is the motivation for the least squares approximation method.

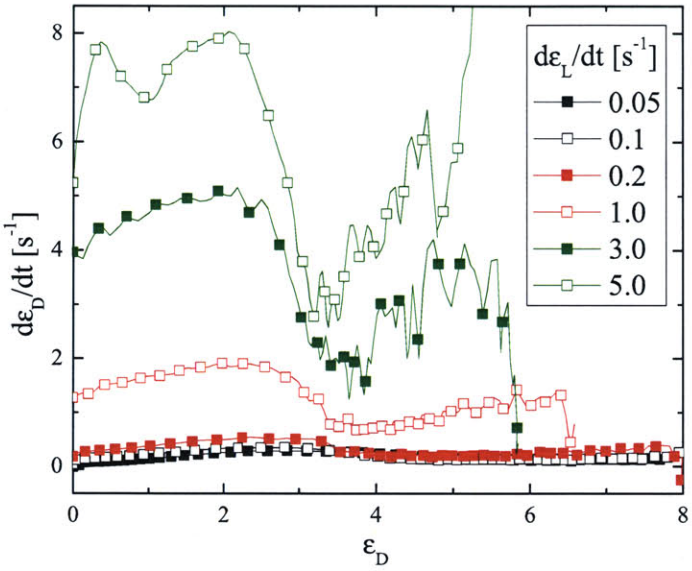

(a) Strain rate

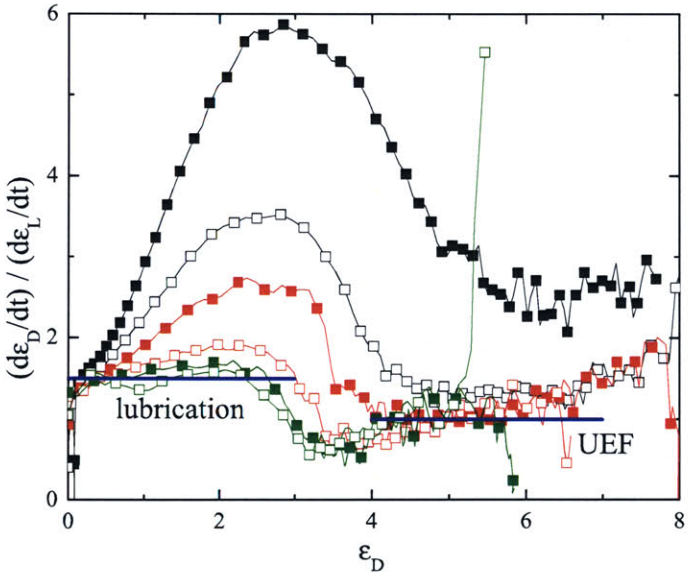

(b) Strain rate normalized by nominal strain rate

Figure 5–7: Radial strain rates, $\dot{\varepsilon}_D$, from type II experiments. (a) shows the raw strain rates, whereas (b) shows the rate normalized by the nominal strain rate, $\dot{\varepsilon}_L$, which is constant for each experiment. The blue lines indicate the value as predicted by lubrication and uniform elongational flow (UEF).

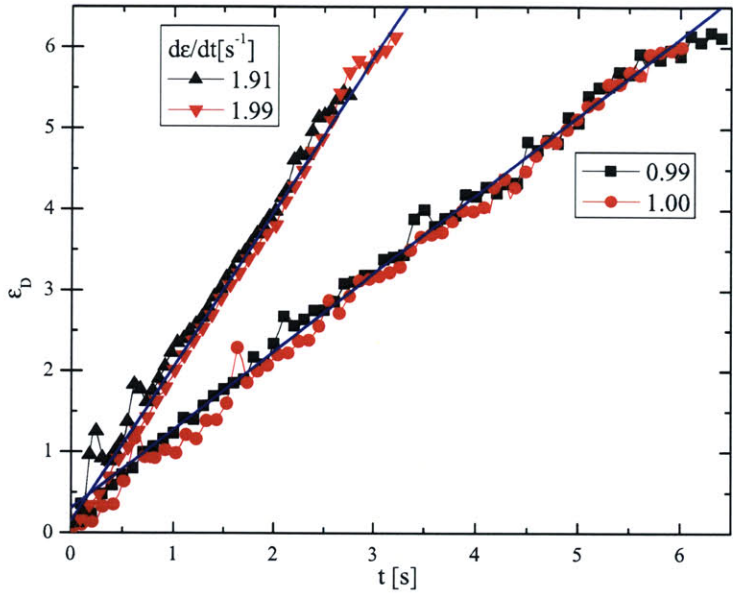

Figure 5–8: Radial strain results from Euler type III experiments. The blue lines are lines of constant strain rates $\dot{\varepsilon} = 0.97$ and $1.91\ s^{-1}$.

5.3.3 Type III Results via Least Squares Approximation

We now present results for type III experiments, this time using the least squares approximation method. The motivation for using this method was to reduce the amount of noise in the data. We want to keep the strain rate as constant as possible. This requires that the endplate positions and velocities are smooth, which is important for reducing the amount of mechanical noise from the motor movement.

Figure 5–10 shows the radius decay from an type III experiment done with the least squares approximation method. In comparison to figure 5–8, the radial strain rates are more constant than they were from the Euler method. Though we see "kinks," the lines maintain their constant slope, meaning that the rates are constant throughout the experiment, even if it is temporarily thrown off course.

Figure 5–11 shows the experimental data collected from type III stretching experiments with their corresponding FENE-PM predictions. Again, the Trouton ratio for earlier times do not follow the $Tr \sim 3\eta_s/\eta_0$ limit as predicted, but is closer to

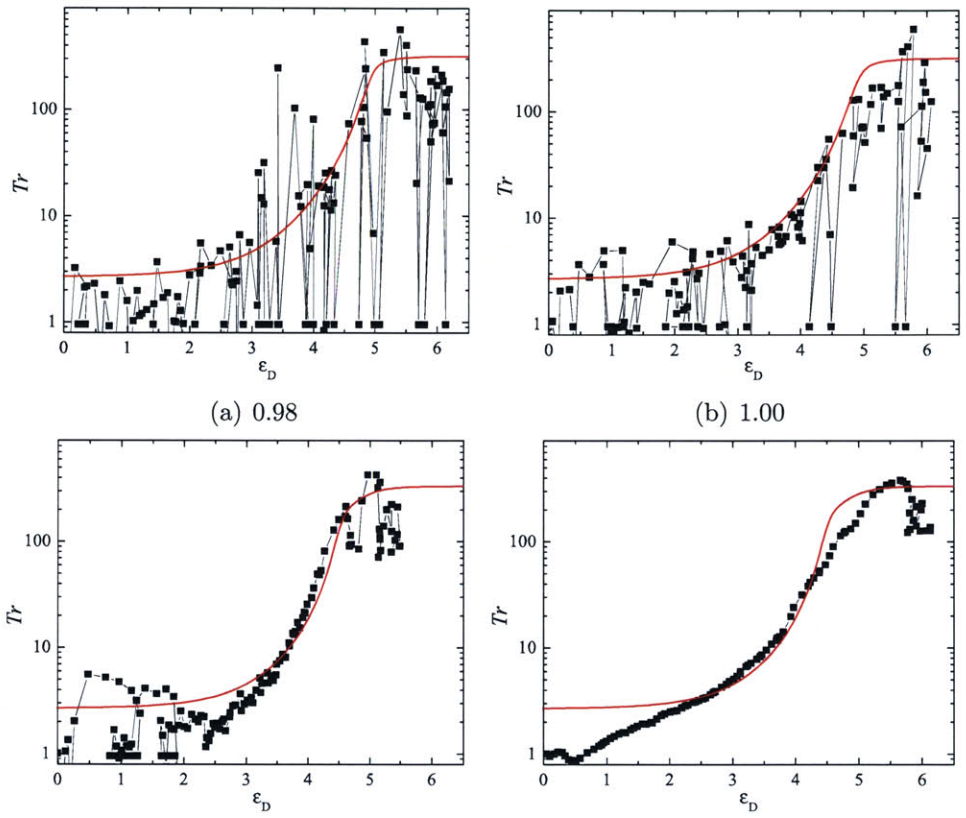

(a) 0.98 (b) 1.00

(c) 1.91 (d) 1.99

Figure 5–9: Trouton ratio, Tr, as a function of radial strain, ε_D, in type III experiment achieved with the Euler method.

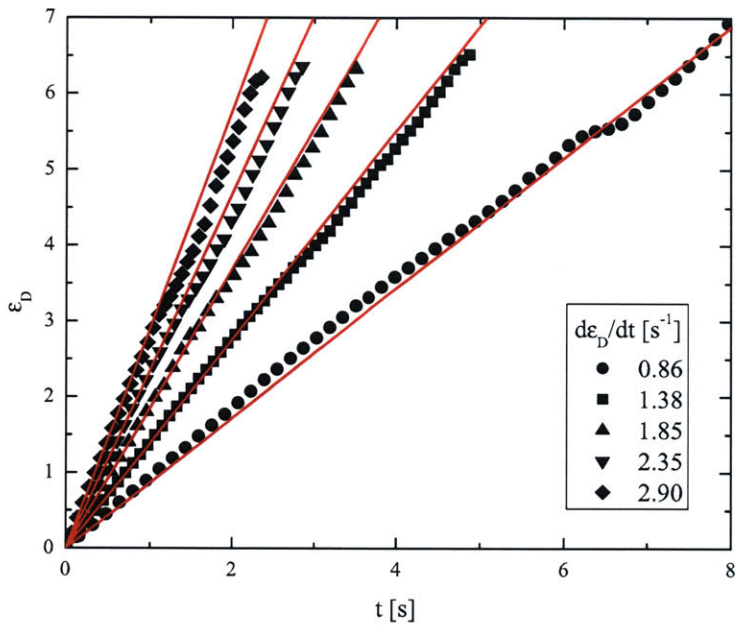

Figure 5–10: Radial strain results from least square approximation type III experiments. The red lines are lines of constant strain rates.

$Tr \sim 1$. Around strains of $\varepsilon_D \approx 1.5 - 2$, the experimental data for Tr increases and starts to follow FENE-PM prediction. The Tr data then grows in close accordance to FENE-PM. The data, however, does not experience a sharp change to steady state. The FENE-PM predicts a steady state Tr to be reached by $\varepsilon_D \approx 5$. Experimental data shows that Tr is still increasing at this strain. The data also do not show a steady state viscosity, and hence, or a steady state Tr. We will discuss this later in section 5.3.4. This is consistent across all five strain rates that were imposed.

As expected, the Trouton ratio, Tr, increases with strain rate. The important parameter is the Deborah number, De. As De stays below the critical value of $1/2$, the force decreases at a rate such that Tr stays constant. As De raises above $1/2$, we start to see stresses tat result from the polymer. Though we do not see results from rates resulting in $De < 1/2$, we do see the increase in Tr with increasing strain rates.

If we compare type II and type III results, we see a marked difference in the transient extensional viscosities. The initial and final approximations are consistent

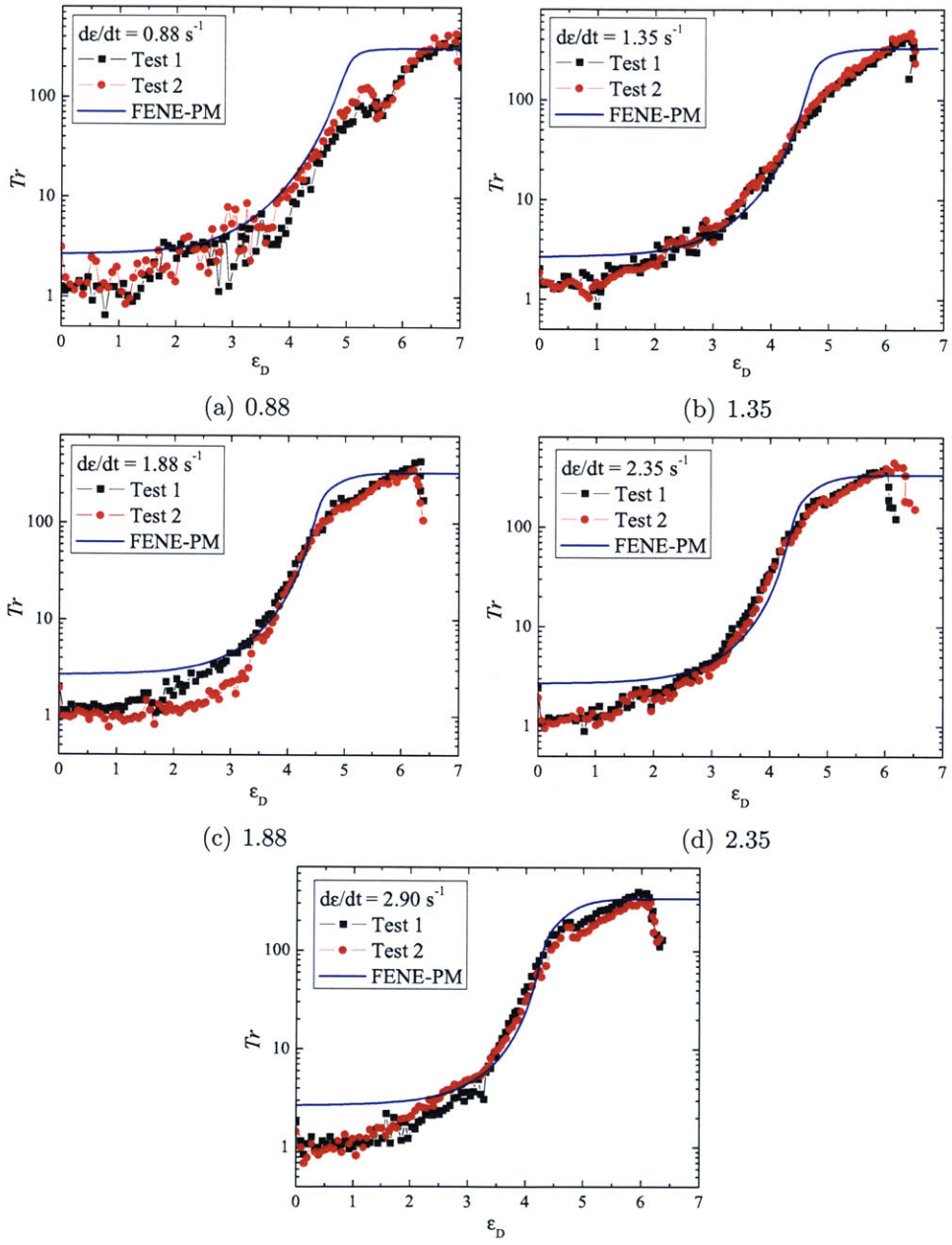

Figure 5–11: Trouton ratio, Tr, as a function of true strain, ε_D.

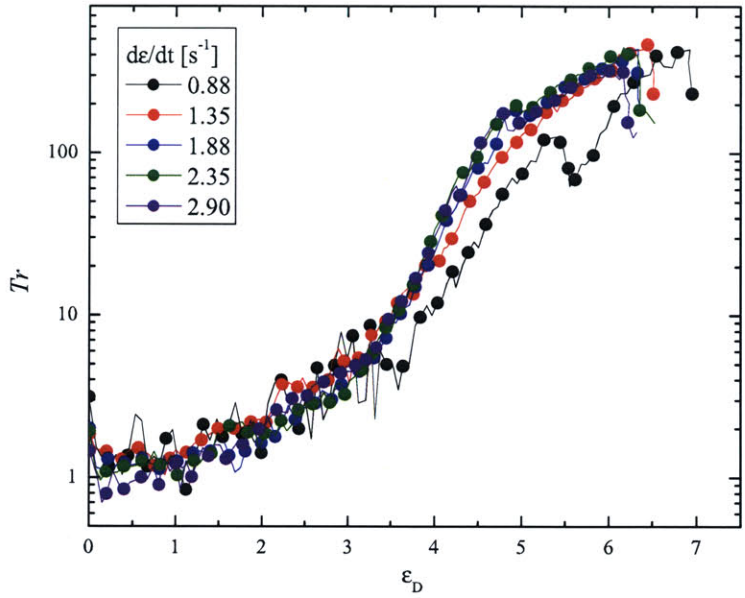

Figure 5–12: Comparison of Tr across all the strain rates.

with each other. The value of $Tr \approx 1$ holds in both types. This is because lubrication holds for both types of stretching experiments since the solvent provides the dominant contribution for the initial stretch. The final extensional viscosity should also be the same for both types because it is governed by the finite extensibility length, which stays the same for a given polymer chain.

The transient is different because the strain rates vary with the two different types. In type II, the axial strain is $L = L_0 e^{\dot{\epsilon}_0 t}$, which means that the diameter will initially deform as $R = R_0 e^{-\frac{1}{2}(\frac{3}{2}\dot{\epsilon}_0)t} = R_0 e^{-\frac{3}{4}\dot{\epsilon}_0 t}$ instead of the $R = R_0 e^{-\frac{1}{2}\dot{\epsilon}_0 t}$ that would result from a type III experiment. Because the polymer chains in a type II stretch experience faster strain rates, the extensional viscosity will be higher.

One alternative to the FENE-PM model to accommodate a type II experiment is to let the true strain rate vary throughout the filament stretching experiment. The strain rate would then be calculated after each an experiment and fed into the FENE-PM calculations. This process of differentiation could add potential sources of noise, but it would capture the higher strain rates due to lubrication in the earlier phases

of a type II stretching experiment. This method would not tell us the dependence of transient extensional viscosity on fixed strain rates. And it also relies on prior knowledge of the fluid deformation. The advantage, however, of a type II experiment over a type III (constant true strain rate) is that the control is much simpler.

5.3.4 Steady State Extensional Viscosity

As FENE-PM predicts, the extensional viscosity of our polymer solution, PS025, does not grow unbounded. At some strain, determined by the extensibility L^2, the extensional viscosity reaches a steady value. We were not able to reach a steady state viscosity in our experiments, both type II and type III. The reason for this is the rapid necking of the filament. Bach *et al.* also observed the same effect. In his study [4], he noted that he could measure a steady state extensional viscosity over as much as two strain units for a slightly strain-hardening LLDPE. In a strongly strain-hardening LDPE, however, the extensional viscosity did not reach a steady state value.

5.4 Lubrication Effects on Initial Conditions

In both type II and III experiments, we see that the initial Trouton ratio does not follow the expected value of $Tr \sim 3\eta_s/\eta_0$. The reason is that at the start of the experiment, the Trouton ratio is governed by lubrication, as the fluid stress is dominated by the solvent. The no-slip condition on the endplates means that there will be shear stresses. From lubrication theory, the fluid exerts a vertical force on the plates. For the case of filament stretching, this is a reverse squeeze flow, so the fluid is pulling the bottom endplate up.

If we say that all the fluid force at time $t = 0$ is from lubrication, then we can calculate the extensional viscosity from the following equation:

$$\eta_E^+ \dot{\varepsilon} \pi R_0^2 = \frac{3\pi\mu V_p(t) R_0^4}{2L_p^3(t)} \tag{5.8}$$

Here, μ is the viscosity of the fluid. Remember that this equation is valid for a

Newtonian fluid, and so we only deal with one viscosity, as opposed to breaking down the viscosity of a polymer solution into polymer and solvent components. The factor V/L can be equated to the strain rate, $\dot{\varepsilon}$. We can then see the limit of η_E^+ at $t = 0$:

$$\lim_{t\to 0} \eta_E^+ = \frac{3\mu}{2}\left(\frac{R_0^2}{L_p^2}\right) = \frac{3\mu}{2}\frac{1}{\Lambda_0^2} \tag{5.9}$$

,

where the aspect ratio is defined as $\Lambda_0 = \frac{L_p}{R_0}$

For the plate size and initial gap length that we use,[2] we would expect the extensional viscosity to be approximately $\eta_E^+ \approx \frac{3}{2}\left(\frac{3.5}{4}\right)^2 \mu = 1.15\mu$. We now say that $\mu = \eta_s$ for our polymer solution at early times. We can then extend this to the Trouton ratio, Tr:

$$Tr\left(\Lambda_0 = \frac{4}{3.5}\right) = \frac{\eta_E^+}{\eta_0} = 1.15\frac{\eta_s}{\eta_0} \tag{5.10}$$

For the PS025 solution across the temperature ranges T $15 - 25°C$, the ratio $\eta_s/\eta_0 \approx 0.9$, giving us a Trouton ratio of $Tr = 1.03$. This is consistent with what we see in both type II and type III experiments at initial times.

This explains why the initial Trouton ratios in figures **??**, 5–11, and 5–12 are approximately unity, as opposed to the $3\eta_s/\eta_0$ as the FENE-PM predicts for uniform elongational stretching. As the radial strain reaches $1.5 - 2$, the apparent Trouton ratio increases above the unity line and approaches the FENE-PM model. In figure 5–13, we see that the force measured by the plates does indeed closely match the lubrication forces for initial times. However, the lubrication forces drop rapidly as L_p in the denominator grows exponentially fast.

[2]The initial fluid radius is usually around 3.5mm, as the endplates are 7mm in diameter, and the initial gap length is set at $L_0 = 4$mm

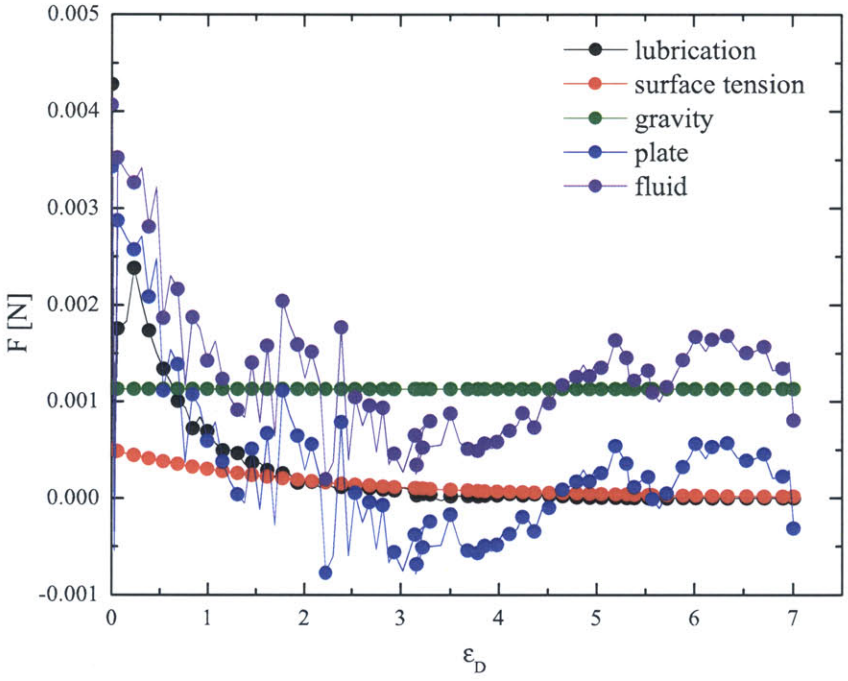

Figure 5–13: Force contributions from various effects. For $t \approx 0$, the force that the plate measures is very close to the force predicted by lubrication theory.

Chapter 6

Break-up of Newtonian and Weakly Elastic Fluids

We now present a study on the break-up of a Newtonian fluid and a weakly elastic fluid. We stretch these fluids under stretch-to-break (STB) experiments. See section 3.4 for some of the previous studies done with STB experiments. For a Newtonian fluid, we propose a force balance, which results in an ODE that can be solved analytically. For the weakly elastic fluid, we compare the results to ODE given by the Newtonian model. A more accurate fit would be to use the second order fluid [6].

6.1 A Proposed Theoretical Model

In STB experiments, the fluid is stretched very slowly. This can either be done with a constant velocity or an exponential trajectory, with the rate so low that the trajectory appears linear.

McKinley [27] provided a force balance for a filament being stretched, but specified a control volume that is different from the one given in figure 3–8. The control volume cuts the fluid away from the endplate, keeping out the region with edge effects. The force balance on this new control volume is given by:

$$\frac{(2X-1)\,\sigma}{R} + \Delta\tau_{ext} - [\tau_{zz}^{p} - \tau_{rr}^{p}] - 3\eta_s\dot{\varepsilon} = 0 \tag{6.1}$$

The factor of $(2X-1)$ is to compensate for the geometry near the endplates. McKinley used the value $X \approx 0.7127$, the Papageorgiou solution. For a Newtonian fluid, equation 6.1 can be simplified, as there is no polymer stress.

$$\dot{\varepsilon} = -\frac{2}{R}\frac{dR}{d\hat{t}} = \frac{(2X-1)\,\sigma}{3\eta_s R} + \frac{\Delta\tau_{ext}}{3\eta_s} \tag{6.2}$$

We can further simplify the force balance by saying that the external stress comes from the fluid undergoing uniform elongational flow, $\Delta\tau_{ext} = 3\eta_s\dot{\varepsilon}$. After some non-dimensionalizing, we get:

$$\dot{h} + Ch + 1 = 0 \tag{6.3}$$

where we use the non=dimensionalized variables $t_{ref} = \frac{6\eta_s R_0}{(2X-1)\sigma}$, $t = \hat{t}/t_{ref}$, $h = R/R_0$. C is defined as $C = \frac{3\eta_s \dot{E} R_0}{(2X-1)\sigma}$ and can be considered an "external capillary number." Equation 6.3 is an ODE and can be solved analytically. We impose the initial condition that $h\,(t=0) = 1$, which implies (from equation 6.3) that $\dot{h}\,(t=0) = -\,(1+C)$. The general solution for the ODE is:

$$h = \frac{1}{C}\left[(1+C)\,e^{-Ct} - 1\right] \tag{6.4}$$

It is good to note some of the limiting cases. When the plates are not moving, *i.e.*, $\dot{E} = 0$, then we get $C = 0$. This leads to $\dot{h} = -1$ and $h = (1-t)$, or $\frac{R}{R_0} = \frac{(2X-1)\sigma}{6\eta_s}\left(\hat{t}_{rupture} - \hat{t}\right)$, which is what we expect from a CaBER experiment. If surface tension becomes negligible, $\sigma \to 0$, then $C \to \infty$. We see from equation 6.2 that the ODE becomes:

$$-\frac{2}{R}\frac{dR}{d\hat{t}} = \dot{E} \tag{6.5}$$

giving us the UEF limit $R = R_0 e^{\frac{1}{2}\dot{E}t}$. If the flow is governed by lubrication, the equation 6.5 changes to

$$-\frac{2}{R}\frac{dR}{d\hat{t}} = \frac{3}{2}\dot{E} \tag{6.6}$$

giving us the lubrication limit $R = R_0 e^{\frac{3}{4}\dot{E}t}$.

6.2 STB Experiments with Styrene Oil

The Newtonian fluid we used was styrene oil. We first measure the shear viscosity of styrene oil. Just as we did with PS025, we need to determine the viscosity dependence on temperature. We can fit the WLF equation to the data so we can interpolate the viscosities at the various intermediate temperatures in which the experiments were performed.

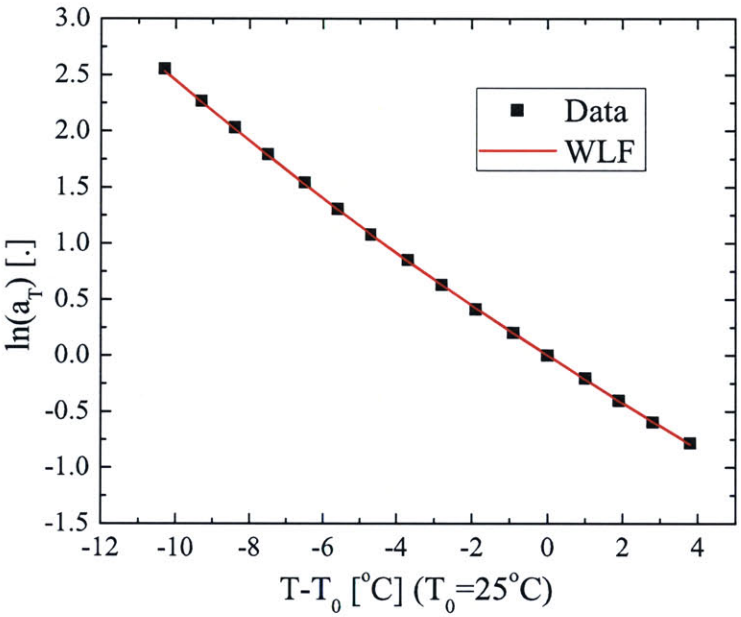

Figure 6–1: Viscosity dependence on temperature, as represented by the function $a_T = \eta(T)/\eta(T_0)$. The experimental data are fit to the Williams-Landel-Ferry (WLF) model, with $c_1^0 = 19.5$ and $c_2^0 = 90.3$. The reference temperature is $T_0 = 25.3°\text{C}$.

Once we have obtained the viscosity of the fluid, we can use it in equation 6.4 to model the break-up. We compare the experimental data with the theoretical model in figure 6–2. We see that there is a huge discrepancy between the data and the theory. Even more troubling is that as the imposed strain rates ($\dot{E}$) increase, the discrepancy increases. We expect that sagging becomes a problem with low rates. For this reason,

we use endplates with smaller radii, 2 mm. This decreases the ratio between the Bond number (Bo) and the Capillary number (Ca), which relates gravitational to viscous effects. Sagging potentially causes the break-up to occur faster, which we see in the data. However, as rates increase, viscous effects increase, and thus the effects of sagging should become smaller. This is not what we see in the results. Note that we could non-dimensionalize the x-axis with t_{ref}, but since t_{ref} does not scale with strain rate, it is relatively constant across the different experiments.

To probe deeper into the discrepancy, we take a look at the strain rates. For the model above, we assume the radial strain rates to be approximately equal to the axial strain rates. Figure 6–3, however, shows the contrary. Even though the radial strain rates are approximately equal to the imposed axial strain rates at initial times, necking causes the radial strain rates to increase by orders of magnitude. We can now explain predict when the theory starts to fail. In figure 6–3, we see that the experimental radial strain rate is approximately equal to the imposed strain rate (bottom-most red line) up to time $t \sim 6$ s. Figure 6–2(a) shows that the experimental data follows the theory up to time $t \sim 9$ s. Similarly, we see that for fastest rate, $\dot{E} = 2\ \mathrm{s}^{-1}$, the experimental radial strain rate is higher than the imposed axial strain rate (top-most red line) from the beginning. And thus we see in figure 6–2(e) that the data never follows the theoretical model.

If we re-calculate the external capillary number, C, with the actual strain rates, calculated from numerical differentiation, we see that the model changes significantly. Because C is now a time-varying variable, h also has to be re-calculated numerically. The model now predicts a faster break-up than the experimental data. This implies that even if there is sagging, the effects are not speeding up the break-up. Though the calculation of the actual strain rate reveals the problem, it does not help fix the model given by equation 6.1, as it is using experimental data in the theory.

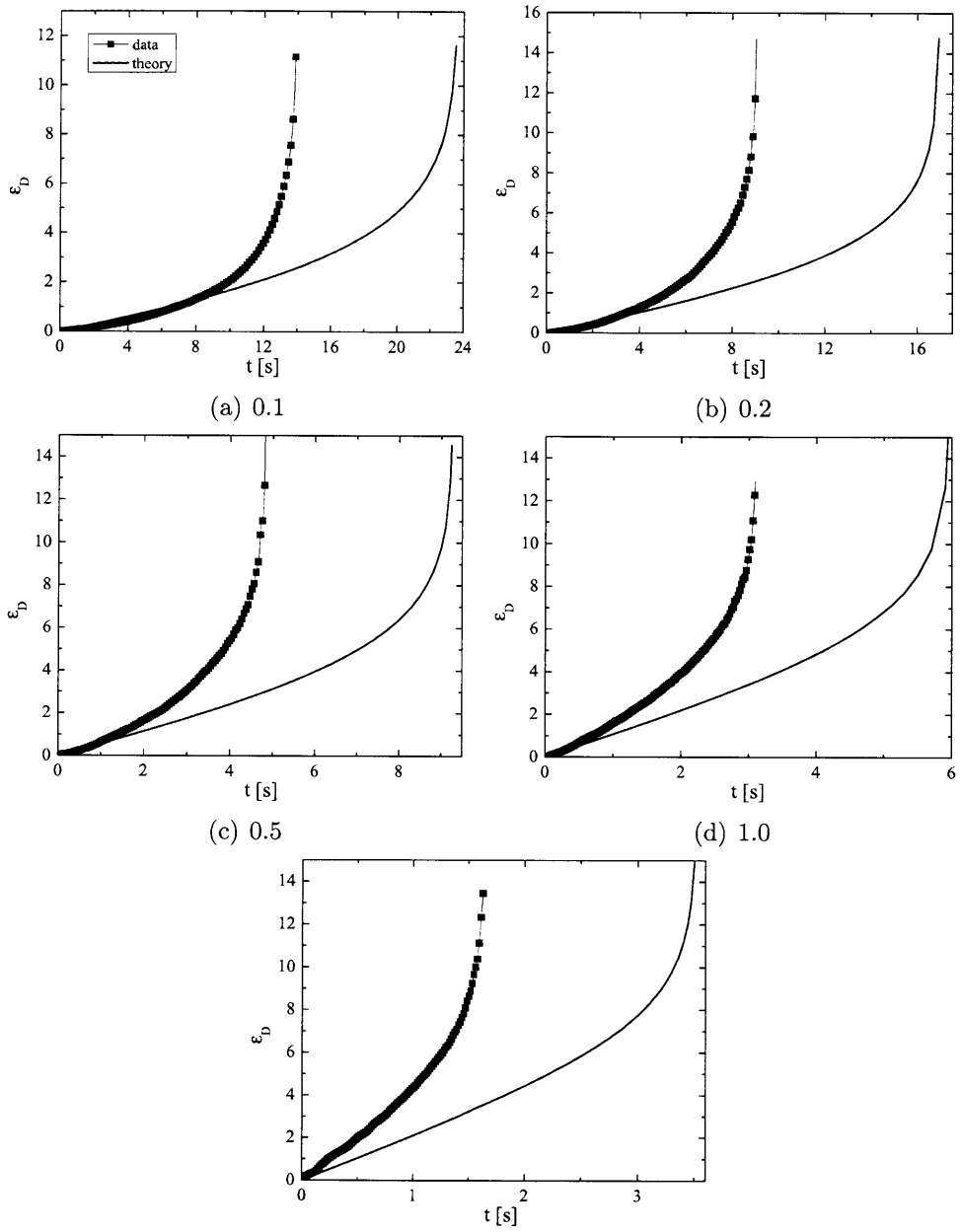

(a) 0.1

(b) 0.2

(c) 0.5

(d) 1.0

(e) 2.0

Figure 6–2: Radial strain of STB experiments, and its comparison to the model as given by equation 6.4.

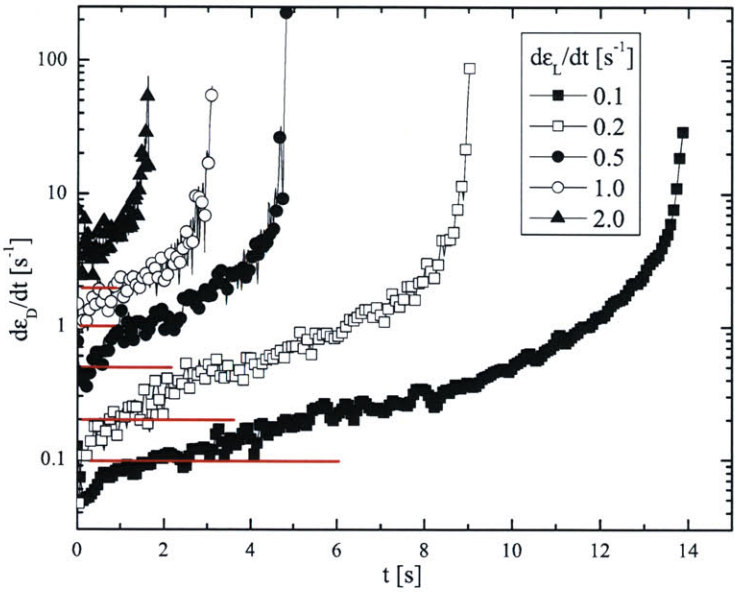

Figure 6–3: Experimental radial strain rates of styrene oil in STB experiments.

6.3 STB Experiments with STP Oil

We now look at the break-up of STP oil, which is a weakly elastic fluid. The simplified force balance, equation 6.2, is no longer valid. However, we can still compare experimental data to that of a Newtonian fluid with the same properties.

Figure 6–5 shows the experimental data with theory for a Newtonian fluid. Again, we show the theory for a fixed C as well as the time-varying C calculated from the actual strain rate.

As before, the theory (with fixed C) predicts a slower break-up than the experimental. The one exception is for the lowest rate, $\dot{E} = 0.05\ s^{-1}$, as seen in figure 6–5(a). For the Newtonian fluid, the theory with a time-varying C predicted a faster break-up than the experimental data. The case is true here as well. However, the disagreement is larger. The elasticity of the fluid prolongs the break-up of the fluid. To quantify the disagreement between the styrene oil and STP, we take a look at the time to break, t_b, of the two fluids. We tabulate the values in table 6.1. For each rate, we have three values for the time to break - the experimental value, the

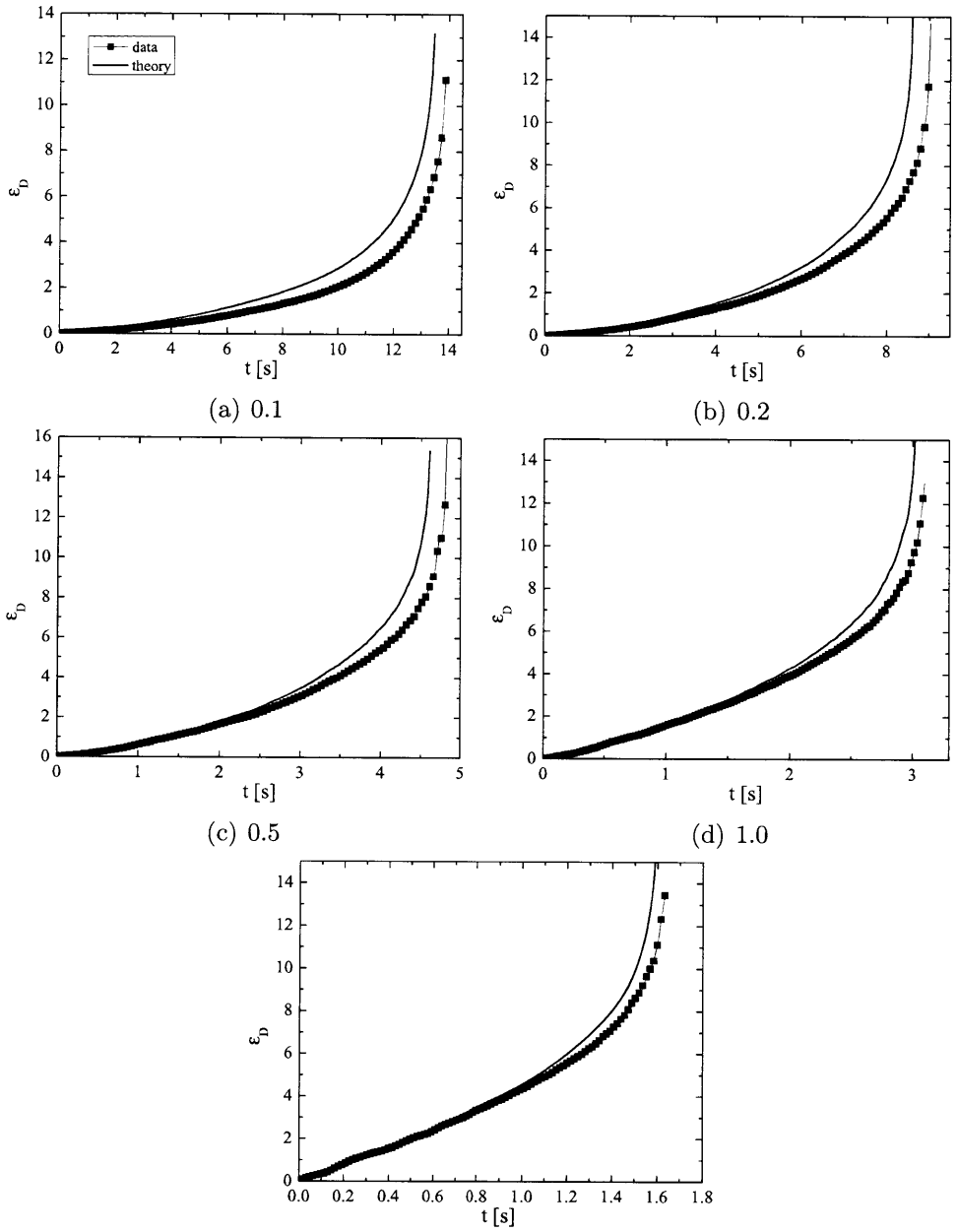

Figure 6–4: Radial strain of styrene oil in STB experiments. The theoretical model is calculated from solving equation 6.3, but using the time-varying values of C from the experiment.

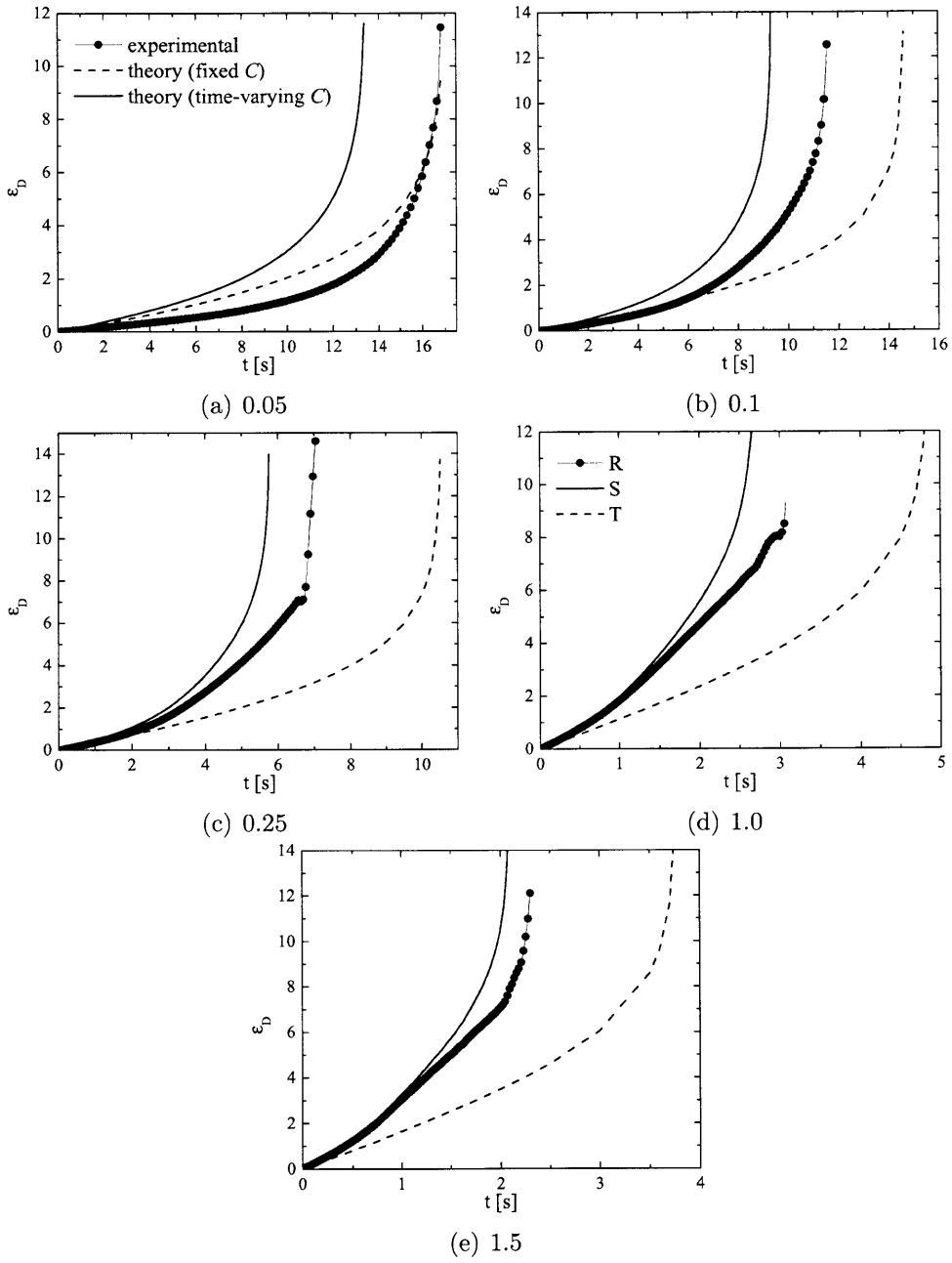

(a) 0.05 (b) 0.1

(c) 0.25 (d) 1.0

(e) 1.5

Figure 6–5: Radial strain of STB experiments, and its comparison to the model as given by equation 6.4.

value from assuming a fixed C, and the value from calculating the break-up with the time-varying experiment C.

Table 6.1: *Time to break, t_b, of styrene oil and STP for different rates.*

Fluid	$\dot{E}$ [s^{-1}]	$t_{b1}^{\dagger}$ [s]	$t_{b2}^{\S}$ [s]	$t_{b3}^{\ddagger}$ [s]	$\frac{t_{b2}-t_{b1}}{t_{b2}}$	$\frac{t_{b3}-t_{b2}}{t_{b2}}$
styrene oil	0.1	13.46	13.87	23.5	0.029	0.694
	0.2	8.62	9.02	16.9	0.044	0.874
	0.5	4.61	4.82	9.24	0.045	0.915
	1.0	3.02	3.10	5.95	0.023	0.921
	1.2	2.39	2.45	5.05	0.025	1.063
	2.0	1.6	1.63	3.5	0.020	1.145
STP	0.05	13.37	16.82	16.82	0.205	0.0
	0.1	9.35	11.56	14.61	0.191	0.264
	0.25	5.77	7.04	10.52	0.181	0.494
	0.5	3.97	5.00	7.31	0.206	0.462
	0.75	3.19	3.74	5.81	0.147	0.555
	1.0	2.69	3.07	4.85	0.125	0.578
	1.5	2.08	2.30	3.75	0.095	0.629
	2.0	1.74	1.84	3.08	0.053	0.672

† Model with varying C.
§ Experimental data.
‡ Model with fixed C.

We compare the differences between the times. We first look at the difference between the experimental and the fixed C theoretical model, normalized by the experimental value. We do the same with the time-varying C model. We see that the the theoretical model with the varying C is closer to the experimental value for styrene oil than it is for STP. Again, this is because the model is for a Newtonian liquid, and the elasticity in STP slows down the break-up. For the fixed C model, the disagreement with the experimental data is greater with the styrene oil. This is because the fixed C model predicts a slower break-up than the experimental data. Since elasticity slows down the break-up, the difference is smaller with STP.

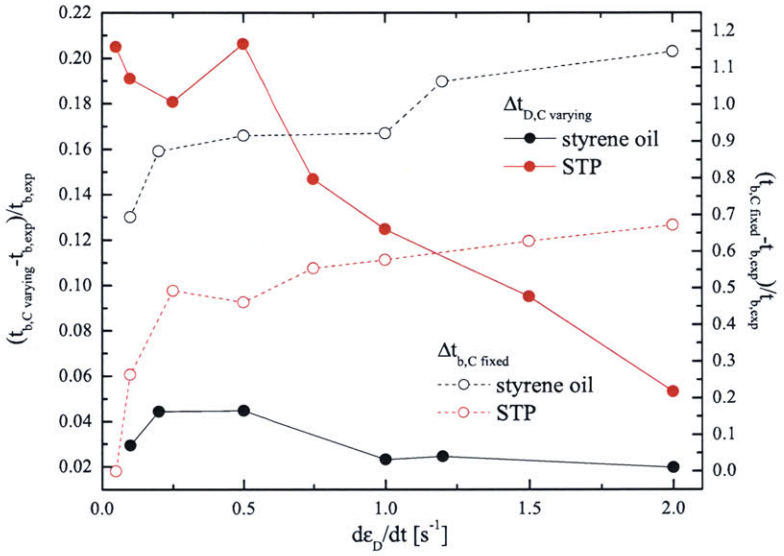

Figure 6–6: Time to break, t_b, of styrene oil and STP. We compare the differences between the experimental and theoretical (both with fixed C and the varying C, with $\dot{E}$ calculated from the experimental data) for various rates.

Chapter 7

Conclusions

7.1 Filament Stretching Type II Experiments

We first ran some type II experiments to show the type of behavior that we expect the Trouton ratio, Tr, to follow. We compare the data to a FENE-PM model that assumes a constant true strain rate. The experimental Tr grows faster than the FENE-PM model. This is because the true strain rates in a type II experiment are actually higher than the imposed axial strain rate, which is fixed in type II experiments, because of lubrication. Therefore, both radial strain and strain rates, which the FENE-PM model is based on, is higher than the assumption taken by the model.

Besides the faster growth of the Trouton ratio, Tr, there is also discrepancy in the initial value of the Tr. Since the polymers in the solution are not "excited" for small strains, we expect the Tr to be governed by the solution, a Newtonian fluid, for small times. This corresponds to a value of $Tr \approx 3\frac{\eta_s}{\eta_0}$, which is approximately 3. However, the data shows values closer to unity. This is explained by the pressure stemming from lubrication flow, which the solution undergoes at small times. From [41], we see that the low value for Tr is consistent with the model, which depends only on the solution and solvent viscosities and the flow geometries, given by Spiegelberg. We further show that the force measurements made are very close to the force required to pull two plates apart with lubrication flow between them.

7.2 Filament Stretching Type III Experiments

We demonstrate a method of achieving type III - constant true strain rate - experiments. We first do this with an Euler method. This method produces a constant strain rate, but the noise in force measurements obscure the data so that the Trouton ratio, Tr, is very noisy as well. We improve this method with the least squares approximation method, where we increase the number of data points taken. In both Euler and least square regression, we take pairs of point containing axial and radial strains to calculate the ratio of the strain rates. We then use the data to calculate the proper amount of axial strain that will result in a constant radial strain rate.

A comparison between the type III data and FENE-PM shows similar trends, but also shows some discrepancy. First, just as with the type II experiments, Tr does not follow the $3\frac{\eta_s}{\eta_0}$ approximation as we would expect. Instead, it is dominated by stresses from lubrication flow. When comparing the data across various strain rates, we see that Tr does indeed depend on strain rate - higher strain rates cause Tr to increase faster. Tr reaches values close to the steady-state value predicted by FENE-PM, but does not stay steady. It always drops steeply as the filament necks. Furthermore, FENE-PM shows the Tr making a "faster" transition to steady-state than the experimental values. See figure 5–11.

7.3 Newtonian Break-up Experiments

We also look at stretch-to-break (STB) experiments of a Newtonian fluid and a weakly elastic fluid. We compare the break-up to a model derived by McKinley. We show that the theory under-predicts the break-up as fluid breaks much faster than the theory. We note that if we use the true strain rate in the theory, rather than the imposed axial strain rate that is held constant, the theory fits the experimental data much more closely.

7.4 Final Comments

While we have introduced a method to achieve type III experiments, there is still much to be done. The least squares approximation has shown that it can control the true (radial) strain well enough to hold the true strain rate constant. However, it is limited to noise from the radius measurements at high strains, when the change in radius is on the same scale as the signal fluctuations. Another limitation is in the force transducer's ability to measure small forces when mechanical noise is present. Improvements can certainly be made in both hardware and software. Using smaller motors will allow the motors to be more easily controllable and reduce some mechanical noise. The caveat is that smaller motors generally produce smaller forces, and hence provide slower acceleration. A force transducer with built-in reference cantilever[1] can help cancel out the mechanical noises. Faster PMAC controllers speeds up the calculation and allow the motion control to be updated more frequently. And finally, more efficient programming and/or more robust control schemes would definitely give us the capability of reaching type III experiments not only at higher strain rates, but also at lower strain rates, where the forces are small and easily blocked out by noise.

[1] Aurora Scientific Inc. makes such transducers. These transducers are physically more delicate and need to be handled with more care.

Appendix A

Appendix

A.1 Sample Code

This is the a sample of the code used to control a type III experiment. In the following example, the least squares approximation method is incorporated. Similar code would be used for the Euler method, with the only change coming in the definition of the slope, $\Delta\varepsilon_L/\Delta\varepsilon_D$. Code is written in the Delta Tau PE Win 32 Pro editor. Lines, or parts of lines, beginning with ';' are used to comment.

```
#include<least_sq_approx.h

;October 30, 2004 modifications
;Set slope to be 1.6 (as it approximately is from experiments)
;Set the first two points to be slightly greater than initial gap
;Reason for this is that we want to get the motors started
;otherwise, asking it to move even 0.05mm from rest requires
;overcoming a certain inertia, causing overshoot (see the position
;plots of commanded and actual positions at the beginning).

;November 2,2004
;Once eL exceeds 4, force the slope to be set at 2, (i.e.40000)

Open Prog 4 clear
;define max height (P856) in mm and save prior to beginning prog
strate_rad = 0.5*strainrate
;should be 0.5 * strainrate, P751=0.5*P750
initD=D_m*diam+D_b
ln_initD = ln(initD)
```

```
ln_initL = ln(initL)
slope=32000
;initialize the slope
COMMAND"del gat"
;delete gathering
COMMAND"def gat"
;define gathering
ABS
linear
TA(piecetime)
TM(piecetime)
timescale=0.001*piecetime

;give 4 pairs of points that will result in lubrication theory
D1=-0.04
D2=-0.02
D3=0

L1=D1*9/5
;should be *4/3 for lubrication
L2=D2*9/5
L3=D3*9/5

;prevD=initD
prevprev_pos=initL+10
prev_pos=initL+20
curr_pos=initL * EXP(1/3 * strainrate*timescale)
;really the prev_prev_pos for the 1st iteration
next_pos=initL * EXP(2/3 * strainrate*timescale)

Command"&1 b5 r"
close

Open Prog 5 clear
;time = 0
COMMAND"GAT"

X(-prevprev_pos)Y(.5*prevprev_pos)
;reads @ t=0
X(-prev_pos)Y(.5*prev_pos)
;reads @ t=dt, happens at t=2*TM
X(-curr_pos)Y(.5*curr_pos)
;reads @ t=TM, happens at t=3*TM
;X(-next_pos)Y(.5*next_pos)
;reads @ t=2*TM, happens at t=4*TM
```

```
time=3
While (next_pos < max_height And next_pos > initL)
;1st iteration reads at t=TA+TM
;eD = x, eL = y, slope = dy/dx
  X(-next_pos)Y(.5*next_pos)
  D4 = -ln(D_m*diam+D_b) + ln_initD
;actually eps_D = ln(D0/D) = ln(D0) - ln(D)
  L4 = ln(abs(M161/(I108*32))) - ln_initL
;actually eps_L = ln(L/L0) = ln(L) - ln(L0)
  slope_num=4 * (D1*L1 + D2*L2 + D3*L3 + D4*L4) -
          (D1 + D2 + D3 + D4)*(L1 + L2 + L3 + L4)
  slope_den=4 * (D1*D1 + D2*D2 + D3*D3 + D4*D4) -
          (D1 + D2 + D3 + D4)*(D1 + D2 + D3 + D4)
  slope = 20000 * slope_num/slope_den
  If (L4 > 4)
    slope=40000
  EndIf

;slope = 20000 *(5 * (D1*L1 + D2*L2 + D3*L3 + D4*L4 + D5*L5) -
; (D1 + D2 + D3 + D4 + D5)*(L1 + L2 + L3 + L4 + L5)) /
; (5 * (D1^2 + D2^2 + D3^2 + D4^2 + D5^2) -
; (D1 + D2 + D3 + D4 + D5)^2)

;slope = # * sum(x*y) - sum(x)*sum(y) / # * sum(x^2)- sum(x)^2
; # is the number of pairs of points
;20000*(ln(curr_pos)-ln(prev_pos))/(-ln(curr_D)+ln(prev_D))
;multiply by factor 2 because we're calculating two points ahead
  If (slope > 70000)
    slope=70000
  EndIf
  If (slope < 10000)
    slope=10000
  EndIf
  next_pos=initL*EXP(strate_rad*timescale*slope/10000+L4)
;curr_pos = initL * exp(L5)
;next_pos=initL*EXP((strate_rad*timescale*time-D5)*slope/10000+L5)
';curr_pos = initL * exp(L5)
;next_pos=curr_pos*EXP((strate_rad*timescale*time-D5)*slope/10000)
;next_pos=curr_pos*EXP((strate_rad*timescale*time-ln_initD+ln(curr_D))*slope/10000)
  time = time + 1
  D1 = D2
  D2 = D3
  D3 = D4
  L1 = L2
```

```
  L2 = L3
  L3 = L4
EndWhile
dwell100
CMD"ENDG"
```

A.2 Header file

;this is the header file for the MIT Fiser system
;Programmer: Roger Yeh
;Date: 10/02/2003

;program variable definitions

```
#define force      M105 ;analog input
#define diam       M205 ;analog input

#define prev_slope     M351 ; previous slope
#define slope          M352 ; for euler method

#define time           m500
#define prevprev_pos   m501
#define prev_pos       m502
#define curr_pos       m503
#define next_pos       m504

#define slope_num      P351 ; for euler method
#define slope_den      P352 ; for euler method
#define slope          P353 ;for euler method

#define L1         P501
#define L2         P502
#define L3         P503
#define L4         P504
#define L5         P505

#define D1         P511
#define D2         P512
#define D3         P513
#define D4         P514
#define D5         P515
```

```
#define strainrate      P750 ; experimental parameter comming from VB applica-
tion
#define strate_rad      P751 ; strain rate of the radius = half the strain rate
#define v0              P759 ; initial velocity

#define initL P760 ;experimental parameter comming from VB application

#define initrad         P762 ;initial radius (3.5mm)
#define ln_initrad      P763 ;natural log of initial gap
#define initD           P764 ;initial diameter
#define ln_initD        P765 ;natural log of initial diameter
#define ln_initL        P766 ;natural log of initial gap

#define piecetime       P770 ;PVT piece time
#define timescale       P771 ;scaling for time (in msec)
#define timescale1      P772 ;scaling for time by factor radius strain rate
#define product         P773 ; gamma*timescale*timescale1

#define rad_m       P790 ;radius calibration, slope (rad = m*PMAC+b)
#define rad_b       P791 ;radius calibration, y-intercept (rad = m*PMAC+b)

#define D_m         P792 ;radius calibration, slope (rad = m*PMAC+b)
#define D_b         P793 ;radius calibration, y-intercept (rad = m*PMAC+b)

#define M1_Jog_Up       P800 ;jog command coming from VB application
#define M1_Jog_Down     P801 ;jog command coming from VB application
#define M2_Jog_Up       P802 ;jog command coming from VB application
#define M2_Jog_Down     P803 ;jog command coming from VB application

#define Actual_Gap      P851
#define M1_Current_Pos      P852
#define M3_Current_Pos      P853
#define M1_Start_Pos    P854
#define M3_Start_Pos    P855
```

Bibliography

[1] S. L. Anna, C. Rogers, and G. H. McKinley. On controlling the kinematics of a filament stretching rheometer using a real-time active control mechanism. *Journal of Non-Newtonian Fluid Mechanics*, 87(2-3):307–335, 1999.

[2] Shelley Anna. *Filament Stretching of Model Elastic Liquids.* PhD thesis, Harvard University, Dept of Engineering Sciences, 2000.

[3] A. Bach, K. Almdal, H. K. Rasmussen, and O. Hassager. Elongational viscosity of narrow molar mass distribution polystyrene. *Macromolecules*, 36(14):5174–5179, 2003.

[4] A. Bach, H. K. Rasmussen, and O. Hassager. Extensional viscosity for polymer melts measured in the filament stretching rheometer. *Journal of Rheology*, 47(2):429–441, 2003.

[5] O. A. Basaran. Small-scale free surface flows with breakup: Drop formation and emerging applications. *Aiche Journal*, 48(9):1842–1848, 2002.

[6] R. B. Bird, R. C. Armstrong, and O. Hassager. *Dynamics of Polymeric Liquids: Fluid Mechanics.* John Wiley & Sons, New York, 1987.

[7] R. B. Bird, R. C. Armstrong, O. Hassager, and C. F. Curtiss. *Dynamics of Polymeric Liquids: Kinetic Theory.* John Wiley & Sons, New York, 1987.

[8] D. V. Boger. A highly elastic constant-viscosity fluid. *Journal of Non-Newtonian Fluid Mechanics*, 3(1):87–91, 1977.

[9] D. V. Boger. Model polymer fluid systems. *Pure and Applied Chemistry*, 57(7):921–930, 1985.

[10] D. V. Boger and H. Nguyen. Model viscoelastic fluid. *Polymer Engineering and Science*, 18(13):1037–1043, 1978.

[11] J. Burnett, F. A. Glover, and G. W. Scott-Blair. Field measurements of the "spinability" of bovine cervical mucus. *Biorheology*, 4:41–45, 1967.

[12] A. U. Chen and O. A. Basaran. A new method for significantly reducing drop radius without reducing nozzle radius in drop-on-demand drop production. *Physics of Fluids*, 14(1):L1–L4, 2002.

[13] F. C. Chretien, B. Ozenda, and B. Volochine. Automatic device for measuring the spinability of cervical mucus in woman. *Med. Biol. Eng. Comput.*, 15(1?):673–678, 1977.

[14] V. M. Entov and E. J. Hinch. Effect of a spectrum of relaxation times on the capillary thinning of a filament of elastic liquid. *Journal of Non-Newtonian Fluid Mechanics*, 72(1):31–53, 1997.

[15] R. H. Fernando, L. L. Xing, and J. E. Glass. Rheology parameters controlling spray atomization and roll misting behavior of waterborne coatings. *Progress in Organic Coatings*, 40(1-4):35–38, 2000.

[16] R. K. Gupta, D. A. Nguyen, and T. Sridhar. Extensional viscosity of dilute polystyrene solutions: Effect of concentration and molecular weight. *Physics of Fluids*, 12(6):1296–1318, 2000.

[17] K. P. Jackson, K. Walters, and R. W. Williams. A rheometrical study of boger fluids. *Journal of Non-Newtonian Fluid Mechanics*, 14:173–188, 1984. Sp. Iss. SI.

[18] R. G. Larson. *The Structure and Rheology of Complex Fluids.* Oxford University Press, New York, 1999.

[19] R. G. Larson. The rheology of dilute solutions of flexible polymers: Progress and problems. *Journal of Rheology*, 49(1):1–70, 2005.

[20] M. E. Mackay and D. V. Boger. An explanation of the rheological properties of boger fluids. *Journal of Non-Newtonian Fluid Mechanics*, 22(2):235–243, 1987.

[21] J. E. Matta and R. P. Tytus. Liquid stretching using a falling cylinder. *Journal of Non-Newtonian Fluid Mechanics*, 35(2-3):215–229, 1990.

[22] G. H. McKinley. A decade of filament stretching rheometry. In *XIIIth Int. Congress Rheol.*, Cambridge, UK, 2000.

[23] G. H. McKinley. Visco-elast-capillary thinning and break-up of complex fluids. *Annual Rheology Reviews*, 3, 2005.

[24] G. H. McKinley, S. L. Anna, A. Tripathi, and M. W. Yao. Extensional rheometry of polymeric fluids and the uniaxial elongation of viscoelastic filaments. In *15th International Polymer Processing Society*, Netherlands, 1999.

[25] G. H. McKinley, O. Brauner, and M. W. Yao. Filament stretching rheometry and the extensional viscosity of dilute and concentrated polymer solutions. In *1st International Symposium on Applied Rheology*, pages 65–71, Korea, 2001.

[26] G. H. McKinley and T. Sridhar. Filament-stretching rheometry of complex fluids. *Annual Review of Fluid Mechanics*, 34:375–415, 2002.

[27] G. H. McKinley and A. Tripathi. How to extract the newtonian viscosity from capillary breakup measurements in a filament rheometer. *Journal of Rheology*, 44(3):653–670, 2000.

[28] N. V. Orr and T. Sridhar. Stress relaxation in uniaxial extension. *Journal of Non-Newtonian Fluid Mechanics*, 67:77–103, 1996.

[29] N. V. Orr and T. Sridhar. Probing the dynamics of polymer solutions in extensional flow using step strain rate experiments. *Journal of Non-Newtonian Fluid Mechanics*, 82(2-3):203–232, 1999.

[30] C. J. S. Petrie. *Elongational Flows: Aspects of the behaviour of model elastico-viscous fluids.* Pitman, London, 1979.

[31] O. Pitois, P. Moucheront, and X. Chateau. Rupture energy of a pendular liquid bridge. *European Physical Journal B*, 23(1):79–86, 2001.

[32] G. Prilutski, R. K. Gupta, T. Sridhar, and M. E. Ryan. Model viscoelastic liquids. *Journal of Non-Newtonian Fluid Mechanics*, 12(2):233–241, 1983.

[33] E. Puchelle, J. M. Zahm, and C. Duvivier. Spinability of bronchial musuc. relationship with viscoelasticity and mucous tranport properties. *Biorheology*, 20:239–249, 1983.

[34] H. K. Rasmussen, J. K. Nielsen, A. Bach, and O. Hassager. Viscosity overshoot in the start-up of uniaxial elongation of low density polyethylene melts. *Journal of Rheology*, 49(2):369–381, 2005.

[35] J. Remmelgas, L. G. Leal, N. V. Orr, and T. Sridhar. Viscous and elastic stresses in extensional rheometry. *Journal of Non-Newtonian Fluid Mechanics*, 76(1-3):111–135, 1998.

[36] W. W. Schultz. Slender viscoelastic fiber flow. *Journal of Rheology*, 31(8):733–750, 1987.

[37] W. W. Schultz and S. H. Davis. One-dimensional liquid fibers. *Journal of Rheology*, 26(4):331–345, 1982.

[38] M. L. Sentmanat. Miniature universal testing platform: from extensional melt rheology to solid-state deformation behavior. *Rheologica Acta*, 43(6):657–669, 2004.

[39] H. J. Shore and G. M. Harrison. The effect of added polymers on the formation of drops ejected from a nozzle. *Physics of Fluids*, 17(3), 2005.

[40] J. J. E. Slotine and W. Li. *Applied Nonlinear Control.* Prentice Hall, New Jersey, 1991.

[41] S. H. Spiegelberg, D. C. Ables, and G. H. McKinley. The role of end-effects on measurements of extensional viscosity in filament stretching rheometers. *Journal of Non-Newtonian Fluid Mechanics*, 64(2-3):229–267, 1996.

[42] T. Sridhar and R. K. Gupta. Fluid detachment and slip in extensional flows. *Journal of Non-Newtonian Fluid Mechanics*, 30(2-3):285–302, 1988.

[43] T. Sridhar and R. K. Gupta. Material properties of viscoelastic liquids in uniaxial extension. *Journal of Rheology*, 35(3):363–377, 1991.

[44] T. Sridhar, V. Tirtaatmadja, D. A. Nguyen, and R. K. Gupta. Measurement of extensional viscosity of polymer-solutions. *Journal of Non-Newtonian Fluid Mechanics*, 40(3):271–280, 1991.

[45] P. Szabo. Transient filament stretching rheometer .1. force balance analysis. *Rheologica Acta*, 36(3):277–284, 1997.

[46] P. Szabo and G. H. McKinley. Filament stretching rheometer: inertia compensation revisited. *Rheologica Acta*, 42(3):269–272, 2003.

[47] D. W. Thompson. *On Growth and Form.* Cambridge University Press, Cambridge, 1961.

[48] V. Tirtaatmadja and T. Sridhar. A filament stretching device for measurement of extensional viscosity. *Journal of Rheology*, 37(6):1081–1102, 1993.

[49] Matthieu Verani. Effects of polymer concentration and molecular weight on the dynamics of visco-elasto-capillary breakup. Master's thesis, Massachusetts Institute of Technology, Dept of Aeronautics and Astronautics, 2004.

[50] K. Walters. Developments in non-newtonian fluid-mechanics - personal view. *Journal of Non-Newtonian Fluid Mechanics*, 5(APR):113–124, 1979.

[51] L. E. Wedgewood, D. N. Ostrov, and R. B. Bird. A finitely extensible bead-spring chain model for dilute polymer-solutions (vol 40, pg 119, 1991). *Journal of Non-Newtonian Fluid Mechanics*, 48(1-2):211–211, 1993.

[52] M. W. Yao, G. H. McKinley, and B. Debbaut. Extensional deformation, stress relaxation and necking failure of viscoelastic filaments. *Journal of Non-Newtonian Fluid Mechanics*, 79(2-3):469–501, 1998.

[53] M. W. Yao, S. H. Spiegelberg, and G. H. McKinley. Dynamics of weakly strain-hardening fluids in filament stretching devices. *Journal of Non-Newtonian Fluid Mechanics*, 89(1-2):1–43, 2000.

[54] O. E. Yildirim and O. A. Basaran. Deformation and breakup of stretching bridges of newtonian and sheer-thinning liquids: comparison of one- and two-dimensional models. *Chemical Engineering Science*, 56:211–233, 2001.

[55] X. Zhang and O. A. Basaran. Dynamics of drop formation from a capillary in the presence of an electric field. *Journal of Fluid Mechanics*, 326(1):239–263, 1996.

[56] X. Zhang, R. S. Padgett, and O. A. Basaran. Nonlinear deformation and breakup of stretching liquid bridges. *Journal of Fluid Mechanics*, 329:207–245, 1996.